

A Method to Determine the Electric Field of Liquid Argon Time Projection Chambers using a UV Laser System and its Application in MicroBooNE

MicroBooNE Collaboration

MICRBOONE-NOTE-1055-PUB

April 29th, 2019

E-mail: microboone_info@fnal.gov

ABSTRACT: Liquid argon time projection chambers (LArTPCs) are today a standard detector technology for accelerator neutrino measurements, due to their high density, precise tracking, and calorimetric capabilities. An electric field (E-field) is required in such detectors to drift ionization electrons to the anode to be collected. The E-field of a TPC is often assumed to be uniform between the anode and the cathode. However, significant distortions can appear from effects such as mechanical distortions, failures, or the accumulation of space charge generated by cosmic rays. The latter is particularly relevant for detectors placed near the Earth's surface and with large drift distances. To determine the E-field in situ, an ultraviolet (UV) laser system is installed in the MicroBooNE experiment at Fermi National Accelerator Laboratory. The purpose of this system is to provide precise measurements of the E-field, and to make it possible to correct for 3D spatial distortions due to E-field non-uniformities. Here we describe the methodology developed for deriving spatial distortions, the drift velocity and the E-field from UV-laser measurements.

Contents

1	Introduction	1
2	Laser System Set-Up and TPC volume scans	2
2.1	Laser Scan	3
2.2	True Laser Track Position	4
3	Reconstruction and Selection of Laser Tracks	5
3.1	Hit and Track Reconstruction	5
3.2	Laser Track selection	7
4	Laser Track Simulations	8
4.1	Toy Simulation	9
4.2	Full Laser Simulation	9
5	Spatial Displacement Map	9
5.1	Spatial Displacement Vectors	10
5.1.1	Closest-point Projection	10
5.1.2	Track Iteration	11
5.2	Boundary Condition	12
5.3	Interpolation	12
5.3.1	Mesh with Delaunay Triangulation	13
5.3.2	Barycentric Coordinates	13
5.4	Sub-Map Merging and Statistical Uncertainty	14
5.5	Bias Study and Systematic Uncertainty	15
5.5.1	Bias Study by Toy Simulation	16
5.5.2	Bias Study by Laser Simulation	17
5.5.3	Coverage of the TPC volume with the UV-laser method	18
6	E-field and Drift Velocity Maps	22
6.1	Field lines	23
6.2	Extraction of the Local Drift Velocity	26
6.3	Extraction of the Local E-field	27
6.4	Validation of the E-field determination	28
7	Measurements in MicroBooNE	30
7.1	Distortion Maps	30
7.2	Drift velocity Map from Laser Data	33
7.3	E-field Map measured from Laser Data	34
8	Time Dependency Studies	37

9	Possible Future Improvements	38
9.1	Hardware Improvements: Future Design of Laser Systems	38
9.2	Analysis Improvements: Maxwell-Faraday constraints	41
9.3	Alternate displacement map determinations	42
10	Conclusion	43

1 Introduction

Liquid argon time projection chambers (LArTPCs) are suitable detectors for neutrino experiments at very large scales. Several massive LArTPCs have already been built and the technology will also be used for the Deep Under ground Neutrino Experiment (DUNE)[1]. MicroBooNE [2] is the first large LArTPC built at the Fermi National Accelerator Laboratory (FNAL) as part of the short baseline neutrino (SBN) program [3]. As the MicroBooNE detector is placed near the surface, space charge effects induced by comparatively slow drifting ions produced by cosmic ray muon interactions can alter the local electric field (E-field). In addition, convection of LAr in the cryostat can further change the E-field. These E-field variations can adversely affect event reconstruction, as ionized electrons experience different drift velocities along their path to the anode and initial ionized electrons have different recombination rates. This further reduces track and energy reconstruction efficiencies of the detector and introduces additional systematic uncertainties. To account for these spatial distortions and measure the E-field together with the drift velocity in MicroBooNE, a novel ultraviolet (UV) laser calibration system has been installed. Unlike cosmic muons, another calibration source, laser beams do not experience multiple Coulomb scattering in LAr. Laser beams can also be repetitively pulsed at controllable direction. Additionally, the UV laser system can be used to investigate detector failures, such as unresponsive or mis-configured wires in the read-out planes.

It has been proven that a UV laser can generate tracks in a LAr TPC through multiphoton ionization [4] [5] [6] [7]. The feasibility of using a UV laser for free electron lifetime measurement in LAr TPC has also been shown [8]. Multiphoton ionization strongly depends on the beam intensity. Argon atoms in the liquid phase can be lifted to an excited state through a laser-induced virtual state by absorption of two UV photons (266 nm). An additional UV photon provides the correct energy to ionize the excited argon atom in liquid phase. A more detailed discussion of this process can be found in [7]. The method using cosmic muons will be described in a separate manuscript.

In section 2, we describe the hardware set-up of the MicroBooNE laser systems, the operation and the result of laser beams scanning over the TPC volume and the calibration of true laser track positions, which are the actual paths of laser beams. The track reconstruction and selection are both optimized for the laser, which is illustrated in section 3. A simulation of laser tracks is described in section 4. In section 5, we describe a complete methodology of computing the spatial displacement maps and their uncertainties. A bias study of the methodology is demonstrated using laser track simulations in the same section. The techniques of extracting E-field and drift velocity for the TPC volume from the spatial displacement map is explained in section 6. The measurement results

of MicroBooNE spatial displacement, drift velocity and E-field maps are presented in section 7. A study of the temporal stability of the E-field is shown in section 8, with distortion measured continuously over a few hours. In section 9, we summarize MicroBooNE's experience measuring E-field using the laser system and we also propose potential improvements in its application in future experiments.

2 Laser System Set-Up and TPC volume scans

The MicroBooNE laser system consists of two identical UV laser sub-systems. One is located upstream of the TPC with respect to the BNB neutrino beam, and the other is located downstream of the TPC. Each sub-system uses a commercial Nd:YAG laser module Surelite I-10¹. The Surelite I-10 initially generates infrared (IR) light (1064 nm), which is shifted to green (532 nm) first, and then UV (266 nm) through second and fourth harmonic generators. The output laser light has most of the intensity in the UV, with significant residual green and IR. The maximum laser pulse repetition rate is 10 Hz. The pulse duration is 4 ns to 6 ns. The UV laser light output of the Surelite I-10 in each pulse has an energy of 60 mJ.

To select only UV light, we use a wavelength separator which is composed of two dichroic mirrors, an attenuator, and an aperture. Figure 1 shows a schematic of the laser systems. The first mirror (M1) has high transmittance for IR light and high reflectance for green and UV light. A beam dump (BD1) at the backside of M1 stops the IR laser light. The second mirror (M2) has high reflectance for UV light while most of the green light is transmitted, terminating at another beam dump (BD3). M2 is mounted on a ZABER T-OMG² motorized gimbal. The gimbal has actuators which provide remote control. Both dichroic mirrors are supplied by Continuum³. In between M1 and M2, there is an Altechna Enhanced Watt Pilot attenuator⁴, which is operating in transmission mode. The attenuation is motorized and can be controlled remotely, with a range of 0.5% to 95% transmittance at 266 nm. It is used to lower and stabilize the laser beam energy. If the energy of the laser pulse is too high or too low, there will be too many or too few ionization electrons to leave a well defined track. A beam dump (BD2) is at the backside of the attenuator to terminate the passing laser. In front of M2, a remote controlled aperture is used to limit the diameter of the transverse laser beam to 1 mm.

A green laser is placed at the backside of M1 in order to reach the same optical path as the UV laser beam. It can give a visual guide for the UV laser beam during alignment and maintenance. A photo diode is used to trigger the data acquisition (DAQ) for laser events when its signal crosses a threshold. Thus, each laser event contains one laser track, unless the beam pulse is blocked by the field-cage rings.

All the optical components mentioned above are contained within a light-tight aluminum "laser box". The output of the laser box is the UV-only beam which is guided to the last warm mirror (M3). It uses the same gimbal as M2, enabling remote control of the mirror angle. The last mirror

¹ http://www.continuumlasers.com/index.php?option=com_content&view=article&id=646&Itemid=574

² <https://www.zaber.com/products/optical-mounts/T-OMG/specs>

³ <http://www.continuumlasers.com>

⁴ <http://www.altechna.de>

(cold mirror) is in LAr and reflects the UV-laser beam into the TPC. It is supported by a 2.5 m-long feed-through. The cold mirror is controlled by two motors⁵, and can rotate both vertically (polar) and horizontally (azimuth). Two independent encoders measure the azimuth and polar angles with high precision. A 2-m-long evacuated quartz light guide allows the UV-laser beam to enter LAr without disturbance at the liquid surface. The cold mirror is within the cryostat but outside of the TPC. It is mounted close to the field-cage rings, which block some beam paths into the TPC. A detailed description of the laser system can be found in [2] and [4].

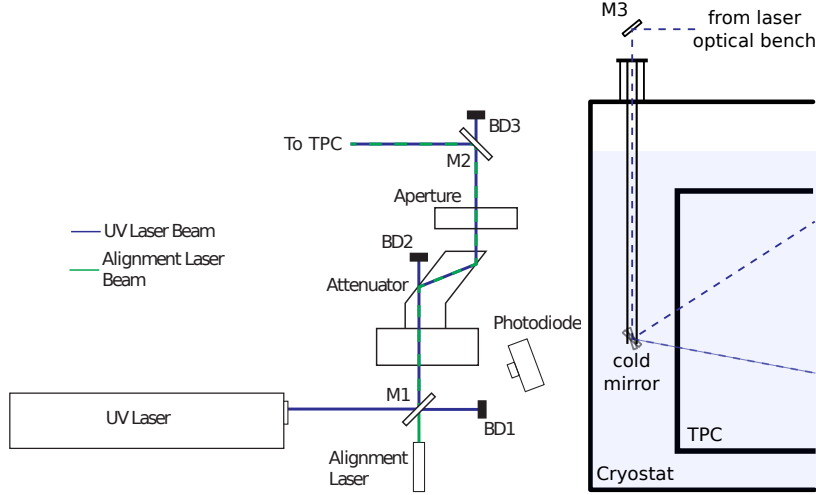


Figure 1. The laser sub-systems at the upstream and the downstream have the same layout. **Left:** Optical path of laser beam before entering the cryostat. The 266 nm laser beam is aligned by two mirrors (M1 and M2), and directed towards the feed through. An attenuator for beam energy control and an aperture for beam size control are placed in between the two mirrors. A photo diode provides a trigger for the readout. **Right:** Schematic of the laser feed through in the cryostat. The UV laser beam reflects at the dichroic mirror M3 and then enters an evacuated quartz tube which serves as light guide to avoid defocusing of the laser beam at the LAr surface. The cold mirror can rotate horizontally together with the feed through assembly. A movable rod extending to a cogwheel allows the cold mirror to rotate vertically. The supporting structure of the cold mirror is mounted to the feed through flange.

2.1 Laser Scan

We use the MicroBooNE coordinate system. The X coordinate is the drift direction, with the anode (readout plane) sitting at $X = 0$ cm, and the cathode being located at $X = 254.4$ cm. The Y coordinate is vertical with a range from -161.25 cm to 161.25 cm, respectively from the bottom and the top of both the cathode and the anode. The Z coordinate is along the beam direction. $Z = 0$ cm is at the upstream end of the TPC closest to the neutrino source and $Z = 1036.8$ cm is the downstream end. These TPC boundaries are the limits of the true spatial coordinates, as the actual TPC active volume.

A full laser scan consists of a range of measurements from both laser sub-systems. The top view (X - Z projection) of a full laser scan pattern with reconstructed laser tracks can be seen in Figure 2. Field-cage rings located in front of the cold mirror obstruct part of the laser beam paths,

⁵<https://thermionics.com/products/manipulators/rnn-rotary-seals/>

which results in the gaps in the laser scan. The TPC corners towards the cathode at the upstream and the downstream ends are not accessible because of the field-cage rings. Laser beams are not aimed in the direction of the anode since photomultiplier tubes (PMTs) and corresponding wavelength shifting plates are mounted behind the anode. To maintain the efficiency of the wavelength shifting plates installed in front of the PMTs, exposure to intense UV light is avoided. In a laboratory measurement at the University of Bern the effect of the beam of the same Surelite UV-laser as employed in MicroBooNE was tested on a plate coated with Tetraphenyl butadiene (TPB). Its effect was found to be negligible. To obtain a noticeable degradation, the full TPB area (5 cm in diameter) had to be directly illuminated at full laser pulse power. Even in this unlikely scenario only a 20% decrease in light conversion was observed after more than 14,000 UV-laser pulses.

In MicroBooNE, the laser scan coverage from both sides is almost symmetric. Slight differences arise from small variations in the attenuator settings between the two sub-systems. In the case of the upstream laser, the laser beams are aimed from 30° to 140° , with respect to the Y axis. The mechanics of the feed through and characteristics of the dichroic mirror limit the range of accessible vertical angle. Horizontally, the laser beams sweep from 45° to 93° , with respect to the X axis. Smaller angles with respect to X are obscured by the field-cage rings. A limit toward larger angles with respect to X is also given by the field-cage rings and the need to avoid the anode.

To achieve a dense scan pattern and to minimize the E-field distortions from the ions induced by the laser beam itself, the pulse repetition rates are limited to 4 Hz. The laser pulses continually while the cold mirrors move. At the beginning of a scan, a laser sub-system is set to an extreme of both horizontal and vertical ranges. Then a horizontal sweep is applied with a speed set to 2000 micro-steps per second ($\sim 0.16^\circ \text{ s}^{-1}$). When the horizontal sweep is complete, the cold mirror tilts vertically without the laser pulsing and then starts another horizontal sweep in the other direction. The attenuator setting is updated based on the laser beam incident angle with respect to the cold mirror, to obtain an appropriate laser beam energy. The cold mirror is a dichroic mirror which has different reflectance at different angles of incidence.

Every time the laser pulses, the photo diode triggers an event. Meanwhile, the position of the cold mirror is read out by two encoders and stored on a local server. Data fragments from the laser DAQ and the TPC DAQ are merged off-line based on the coincidence of their time stamps. Both of their DAQ time clocks are provided by a common Network Time Protocol(NTP) server.

2.2 True Laser Track Position

True laser tracks represent the paths of laser beams in the TPC which are equivalent to the intrinsically straight laser tracks without any E-field distortions. In the TPC, laser tracks are similar to tracks from charged particles. Ionized electrons drift in the same E-field, so reconstruction of ionizations at the same position always leads to a fixed read-out position. Thus, laser tracks can be used to calibrate distortions in the TPC relating to the E-field.

True laser track positions are provided by the reflection point on the cold mirror and the angles at which the laser beams cross the TPC. The reflection point and crossing angle provide laser entry and exit points of the TPC.

The precise position of the reflection point is determined by measuring the ionization pattern caused by the shadow that the field-cage rings cast on the laser scan. This procedure is illustrated in Figure 3. From the engineering drawings, the location of the cold mirror is known to a precision

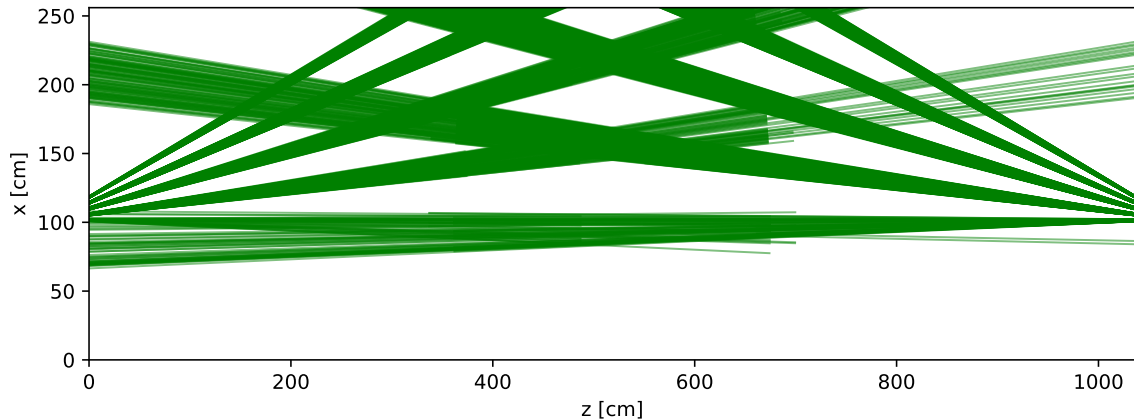


Figure 2. Top view (X - Z projection) of reconstructed laser tracks (green lines) for both laser sub-systems in the TPC active volume. The laser beams are sent into the TPC from the upstream end (left) and the downstream end (right). The laser tracks shown in the plot pass the selection stage described in Section 3.2. Some tracks are cropped because the corresponding laser light exits the TPC at the top surface or the bottom surface. Gaps in the coverage arise due to the presence of field-cage rings in front of the cold mirror.

Sub-system	X [cm]	Y [cm]	Z [cm]
Upstream	103.8 ± 0.05	8.6 ± 0.05	-35.6 ± 0.05
Downstream	102.5 ± 0.05	8.2 ± 0.05	1080.2 ± 0.05

Table 1. Coordinates of the laser reflection point on the cold mirror of the upstream and downstream laser sub-systems, with uncertainties.

of $O(1 \text{ cm})$, which provides a starting point for the fit of the exact position. In MicroBooNE there are 63 field-cage rings supported by horizontal G10 beams [2]. A slow horizontal scan is applied, producing a dense scan pattern. From this pattern, the sharp edges of the field-cage rings and their separations are apparent. A 2-D (X - Z) fit then determines the X and Z positions of the laser reflection point on the cold mirror. The vertical position (Y) is determined using the same technique with a 1-D fit of the horizontal G10 beams' shadow. The calibrated positions of the laser reflection points are listed in Table 1, where we adopted the MicroBooNE coordinates for simplifying the following discussion.

The angles of the laser beams are deduced from the cold mirror positions. As described previously, the cold mirror angles (azimuth and polar) are measured by two independent encoders to a high precision. Position accuracy of true laser tracks is $O(1 \text{ mm})$ at the full distance of 10 m in the TPC.

3 Reconstruction and Selection of Laser Tracks

3.1 Hit and Track Reconstruction

The laser reconstruction procedure first defines a region of interest (RoI), significantly reducing computing time. Hits are then reconstructed within the RoI. These hits are then used for track

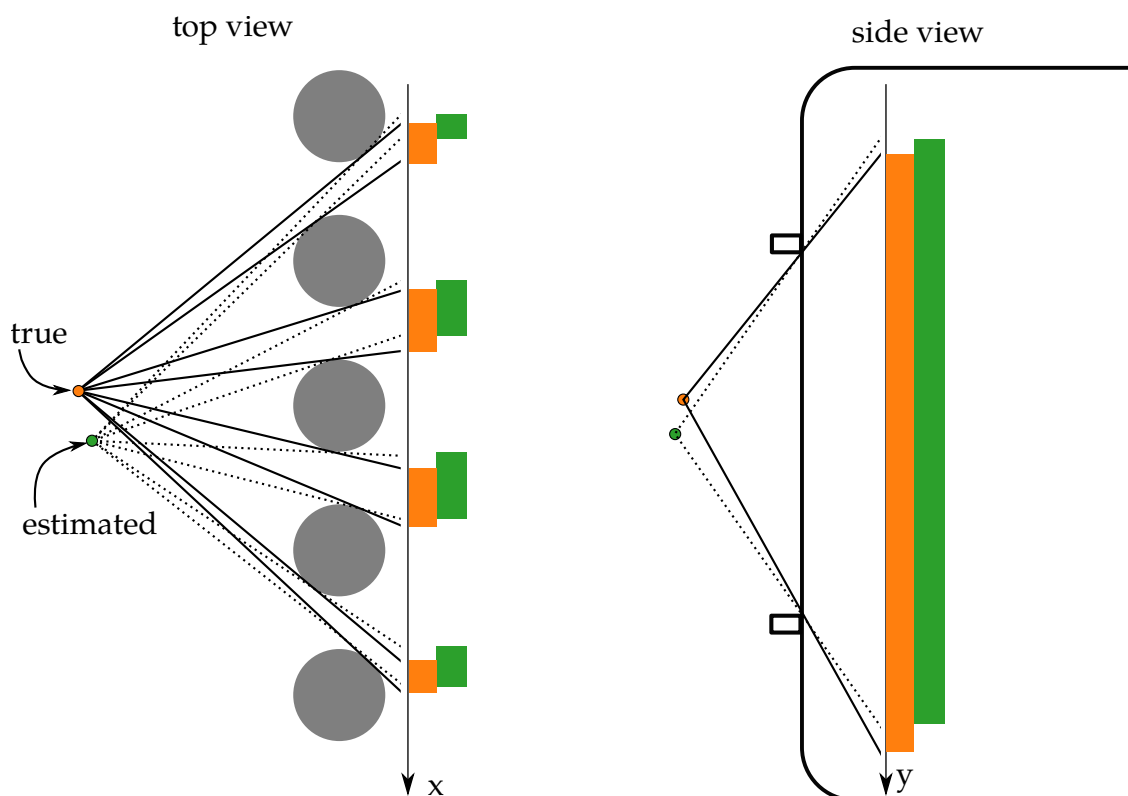


Figure 3. Schematic of the calibration procedure used to determine the position of the laser reflection point on the cold mirror. **Left:** Top view near the cold mirror showing the determination of the laser reflection point on the cold mirror horizontally in the X - Z plane. The gray circles are the cross-section of the field-cage rings. A horizontal scan produces a pattern in the TPC and it is represented by the orange boxes at the TPC edge. Any different reflection point in the X - Z plane would leave a different pattern in the horizontal scan, for example like the green boxes. By fitting the X and Z coordinates of the reflection point, the position of the reflection point on the cold mirror is determined. **Right:** Side view next to the cold mirror showing the determination of the laser reflection point on the cold mirror in Y . The two boxes with solid line are the G10 supporting bars. A vertical laser scan leaves a pattern in the TPC represented by the orange (green) bar for the orange (green) beam reflection origin. A fit to the pattern reveals the true reflection point coordinate in Y . The determination of laser reflection point follows the order of horizontal coordinates (X and Z) first, and then the vertical coordinate (Y).

reconstruction.

The MicroBooNE charge readout consists of two induction-wire planes and one collection-wire plane. For all three planes, the wire pitch is 3 mm. The read-out wires are indexed by wire IDs. Raw signals are waveforms on each wire with respect to the drift time; details of signal processing are described in Ref [9][10]. The hit reconstruction identifies hits as the peak amplitudes and times of waveforms associated to wire IDs. The track reconstruction then employs the hits as an input, grouping them to form 3D space points. Reconstructed track objects are a sequence of 3D points with spatial coordinates in X , Y and Z .

Hit and track reconstructions for the laser employs LArSoft [11], which is the standard software

toolkit for simulation and reconstruction used in MicroBooNE.

An RoI is defined around the true laser track wire IDs and drift time. Given a spatial position in the TPC, LArSoft provides the expected wire ID for each plane. Thus, a range of wire IDs along the true laser track can be identified. The RoI is extended by ± 100 wires (30 cm) around each wire to account for E-field distortions. Similarly, the X coordinate can be converted into time ticks. The RoI in drift time is also determined by the X coordinates of the true laser track, and extended by ± 20 cm. For simplicity, the extensions to the RoI for both wires and drift time remain the same across all events.

With this, hits can be reconstructed inside the RoI. A hit contains information about waveform peak amplitude, width, time, and the associated uncertainties. Typical signals in the collection plane are a single positive peak, whereas signals in induction planes are bipolar peaks. After a baseline correction, a hit is defined when the waveform amplitude is above a threshold and falls back below the threshold. In the collection plane, the time of the highest peak amplitude is defined as the hit time. In the induction planes, the average of the two bipolar peak times is taken as the hit time. For a laser track, the charge deposition is large and the waveform is broadened to a more undefined peak. In this case, the local center time of the peak is taken as the hit time. If the ratio of height to width is too low, the waveform is not reconstructed as a hit. This hit reconstruction algorithm was developed specifically for laser track reconstruction. The conventional hit reconstruction involves waveform deconvolution which has difficulties with the large charge deposition of laser tracks⁶.

The collection of hits can now be used as an input for the Pandora [12] reconstruction tools embedded in LArSoft. In LArSoft version v06, Pandora is composed of *PandoraCosmic* and *PandoraNu* for cosmic or neutrino hypotheses. Since laser beams leave muon-like tracks, *PandoraCosmic* is used for track reconstruction in laser events. Tracks are TPC objects distinguished by separate origins, represented by groups of 3D space points.

3.2 Laser Track selection

A track reconstructed within the RoI may be contaminated. To select a pure laser track, crossing cosmic muons and poorly- or mis-reconstructed laser tracks must be removed. Three selection criteria are applied to the reconstructed tracks as illustrated in Figure 4.

The first two selections are used to eliminate cosmic tracks. In the first selection, tracks only pass if one of the reconstructed track ends is close to the true laser start. The permitted differences in X , Y , and Z are 20 cm. No constraint is applied to the true laser end point, as unresponsive wires or cosmic muons may cause difficulties reconstructing a full laser track.

The second selection compares the angle of the track to the true laser track. Tracks have 3D space points defined by the wire pitch, every 3 mm, for example a 5 m-long track has about 1600 space points. To account for curvature along the track, the first and last 100 space points are used to fit two straight lines. The angles of the lines from each end of the track are then compared to the true laser track angle. The track is selected if both angles are less than 40° from the true track angle.

Only laser tracks survive the above two selections. The final selection step provides a quality control for the reconstructed laser tracks. In MicroBooNE, the possible sources of E-field distortion

⁶Minimum ionizing particles have narrower and shorter waveforms than laser waveform signal.

are space charge and detector deformation. Therefore, no drastic E-field distortion is expected, which means any hard kinks or wiggles in reconstructed laser tracks are not due to E-field related artifacts (Figure 4). The large charge deposition and broad waveforms of the laser introduces uncertainties in the hit reconstruction which can eventually lead to large deformities in the reconstructed track. *PandoraCosmic* can also confuse a short crossing track (cosmics) as a Michel electron. We sort 3D space points in the laser tracks by their ascending Z coordinate. Using the true angle and the separation in Z between neighbouring 3D space points, expected separations in X and Y can be computed. A track fails to pass the selection, if X or Y separations are more than three times larger than expected for ten or more space points. For simplicity, the mis-reconstructed track is removed from the selection, but one could potentially recover the well reconstructed portion of the track for a future selection.

We only use laser track spatial information for calibration, so no requirement on reconstructed laser energy has been applied. From a laser scan taken in the summer of 2016, there are 911 upstream and 1204 downstream tracks after selection. These laser tracks are the input for the following calibration.

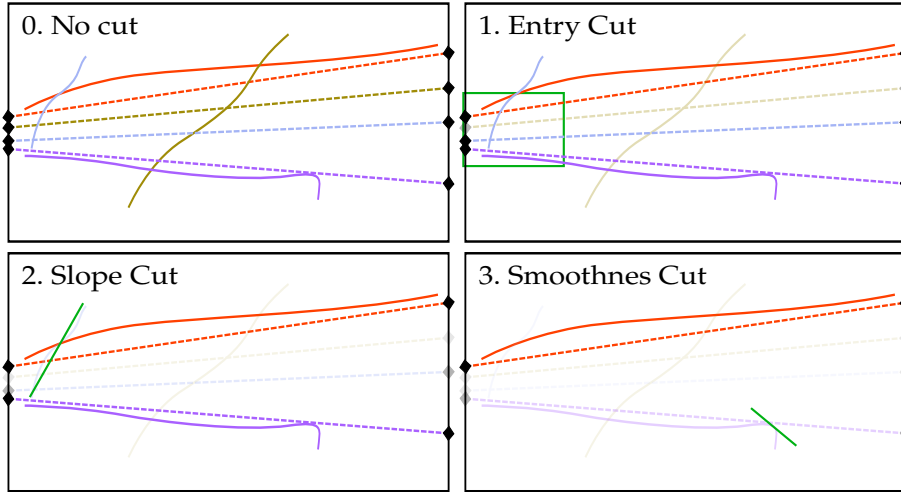


Figure 4. Illustration of the track selection steps. This example uses laser events originated from the upstream laser sub-system. The Z axis is along the horizontal direction, and the vertical axis can be X or Y in these cartoons. The black points on the left hand side of each TPC projection are the laser entry points in the events, and the ones on the right side are the laser exit points. The dashed lines connecting these points are the true laser beam positions. The solid lines with the matching colours represent the possible reconstructed tracks in the corresponding events, which are different due to E-field distortions. (0) Reconstructed tracks have no selection applied. (1) Tracks pass this selection if one of the track ends is within a $20\text{ cm} \times 20\text{ cm} \times 20\text{ cm}$ region from the laser entry. (2) Tracks pass this step if the angles of the first hundred and the last hundred space points are within 40° of the true laser track angle. (4) Tracks pass this cut if no hard kinks or wiggles, due to mis-reconstruction, are present.

4 Laser Track Simulations

Two simulations are used: A toy simulation evaluates the performance of the methodology with ideal tracks and a perfectly known spatial distortion. A more complete laser simulation verifies the

calculation of the spatial-displacement map and the E-field map, and provides an estimate of the systematic uncertainties of the calibration maps.

In both simulations, a “muon gun” is used to replicate true laser tracks in the *Geant4* [13] stage of LArSoft (*LArG4*), with processes such as delta electron emission and multiple Coulomb scattering disabled. True tracks are the simulated laser tracks, and the distorted tracks are the reconstructed laser tracks. No additional cosmic ray muons are simulated.

Initially an E-field distortion is simulated with the charge distribution of positive ions accumulating along X towards the cathode. The corresponding spatial displacement is simulated parametrically. The simulated E-field and spatial displacement are embedded in LArSoft, with spatial distortions being applied to true tracks via LArSoft.

4.1 Toy Simulation

To avoid being biased by the uncertainties from the laser system and the reconstruction, we use the toy simulation to test the methodology. We only use track positions to calculate the spatial displacement, the corresponding local drift velocity and the E-field.

Spatial distortions are applied directly to the true tracks, with the applied offsets deduced from the known E-field. The raw waveform generation and their reconstruction are not simulated. However, simulated tracks are still processed through the track selection described in Section 3.2.

4.2 Full Laser Simulation

To verify the complete chain of the E-field calculation using the laser system, a full laser simulation is introduced to mimic the reconstructed laser data with most of the procedures in place.

This provides more comprehensive track information than the toy simulation by including the reconstruction and selection procedure, which allows us to assess reasonable systematic uncertainties. To eliminate additional systematic uncertainties, the simulated tracks are given the same track angles as the laser data in the scan described in Section 2.1.

In practice, laser beams have a diameter of about 3 mm. The longitudinal diffusion of drifting electrons in the laser simulation is increased to be comparable with the larger beam diameter. To compensate the larger diffusion of ionizing electrons and to represent the greater ionization of laser beams, a scaling factor is applied to the ionization yield. The scaling factor is chosen to allow the simulated laser signal (raw waveform from wires) to match typical laser track data, with a peak voltage of $U_{\max} \approx 80$ mV and time spread of $t_s \approx 10$ μ s.

Afterwards, the simulated laser signals are processed through the reconstruction and the track selection criteria, as described in Section 3.

5 Spatial Displacement Map

Due to a distorted E-field, the position of reconstructed charges in the TPC differs from the true position. Spatial displacement maps are used to show the difference of the reconstructed and the true positions. There are two types of spatial displacement maps which are used in different cases: a distortion map and a correction map.

The distortion map is based on the true spatial coordinates, in which the TPC boundary is regular. It shows the expected reconstructed space points given by the true space points. It can be

used in the simulation of TPC events with E-field distortion. We use it to verify the calculation by comparing it to the simulation truth.

The correction map is based on the reconstructed spatial coordinates, in which the TPC boundary is likely irregular. It shows the expected true space points given by the reconstructed space points. It can be used to calibrate the position of reconstructed TPC objects in a distorted E-field and it is used to derive the local E-field.

For an irregular E-field, it is not trivial to convert from the distortion map to the correction map. However, they contain related information and have many similarities.

For simplicity, the displacement maps are arranged as a regular grid. Therefore, any reconstructed position within the TPC can be translated into the corresponding true position by interpolation between points on the displacement grid. We set 26 bins in X , 26 bins in Y and 101 bins in Z , with the first and last bins centred at the TPC boundaries. For example, along the X axis, the first bin centre is at $X = 0$ cm, and the last bin centre is at $X = 254.8$ cm. The bin size is about $10 \text{ cm} \times 10 \text{ cm} \times 10 \text{ cm}$, but could be made finer if required.

5.1 Spatial Displacement Vectors

Spatial displacement vectors represent the difference between the reconstructed and the true positions. The reconstructed positions are deduced from the positions of the charge read out with the assumption that electrons drift in a nominal and uniform E-field. In practice, the E-field in Micro-BooNE is distorted. The true positions are where the charged particles are physically supposed to be in the TPC. The distortion vectors are measured from the points on the true laser tracks to their corresponding reconstructed points. Alternatively, the correction vectors are measured from the points on the reconstructed tracks to their corresponding true points. Therefore, at this stage with true laser tracks and reconstructed laser tracks, the distortion vectors and the correction vectors have opposite direction with the same length.

The most unambiguous way of calculating the spatial displacement vectors would be to use the crossing-track method. If the E-field does not change, a true position should always be reconstructed in the same position. Because E-field lines cannot cross each other, the true positions and the reconstructed positions have a one-to-one correspondence. The intersection point of two true tracks in a position, with a small tolerance allowed, must correspond to the intersection point of their associated reconstructed tracks. It is therefore straightforward to extract the spatial displacement for those intersection points. However, given the limited TPC coverage and total numbers of laser tracks, it is rare to have crossing tracks.

Without crossing tracks, the difficulty in determining the displacement vectors comes from lacking a point-to-point correspondence. Even though the true laser track positions are known explicitly, it is not straightforward to establish where an associated reconstructed laser track should be. This subsection introduces an alternative method using closest-point projection and track iteration to determine the spatial displacement vectors.

5.1.1 Closest-point Projection

The closest-point projection is a simple way to give a good initial estimation on the spatial displacement vectors. We project reconstructed track points perpendicularly to the true track in 3D; an example of this is shown in Figure 5. The vectors from the reconstructed track points (red) to their

closest point on the true track (blue) are the correction vectors. The vectors with opposite directions starting from the true track (blue) to the reconstructed track points (red) are the distortion vectors.

Calculating spatial displacement vectors by closest-point projection alone introduces a dependency on the laser beam angles. It forces the displacement vectors to be perpendicular to the corresponding true laser tracks. We use a track iteration to reduce the bias from the initial laser beam angles.

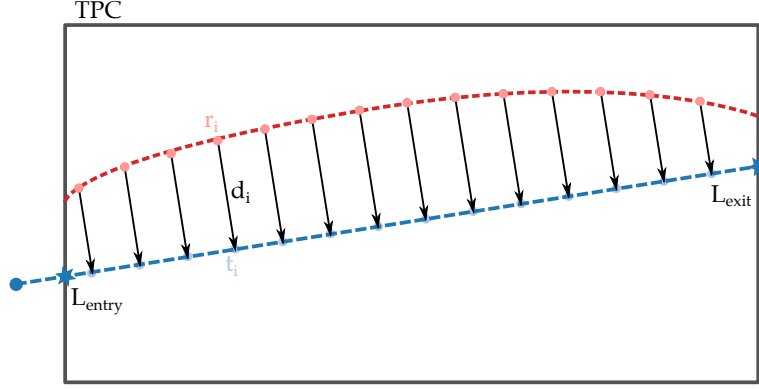


Figure 5. Diagram illustrating the closest-point projection used as the first step in calculating the spatial displacement vectors. The black box is the TPC active volume in true spatial coordinates. Z is along the horizontal direction, and the vertical direction can be either X or Y . The example shown here has a laser beam originating from the upstream sub-system, with the true laser track shown as the blue dashed line in between the laser entry and exit points. The blue dot is the reflection point on the cold mirror which is outside of the field-cage rings. The collection of red dots is the reconstructed track. Each reconstructed point (red dot) r_i is perpendicularly projected to the true laser track in 3D. Its corresponding point on the true track is t_i . The displacement vector starting from r_i to t_i is the correction vector, as shown in the diagram. The distortion vector has the same length but opposite direction as the correction vector. It is based on t_i .

5.1.2 Track Iteration

Based on the closest-point projection, the track iteration improves the calculation of the displacement vectors by reducing the track angle dependencies. Using tracks with a variety of angles reduces the bias.

A complete description of the angles of the used laser tracks can be found in Section 2.1. To maximize the spread in track angles for the correction, we split the laser tracks by their original system. Laser tracks initiating from the upstream sub-system are assembled in track sample **A**, and laser tracks initiating from the downstream sub-system are assembled in track sample **B**. Briefly speaking, we use tracks from one sub-system to calculate the displacement vectors of the other in several iterative steps.

We illustrate the procedure using the example of an n -step iteration with track samples **A** and **B**. At the beginning of the first step, we calculate the correction vectors of track samples **A** and **B** using closest-point projection. Then $\frac{1}{n}$ of the calculated correction vectors of track sample **A** are assigned to the corresponding reconstructed track points. We interpolate the partial correction vectors of track sample **B** with the mesh of all the reconstructed track points in sample **A** and their partial correction vectors. Details of meshing and interpolation methods are explained in Section 5.3. The

inverted procedure is applied here. The partial correction vectors of track sample **A** are interpolated from track sample **B**. By the end of a step, all the track points of both track samples are moved to the intermediate positions where the partial correction vectors point to. At each step of the iteration the above procedures are repeated. The correction vectors calculated at the beginning of a step are taken from the intermediate track positions. For normalization, the partial correction vectors of the track sample **A** (**B**) in a particular step i are interpolated from $\frac{1}{n-(i-1)}$ of the calculated correction vectors. Eventually, in the final step, all the track points from both samples are projected to their closest points on the corresponding true tracks. This guarantees that the displacement vectors link the reconstructed track points to the corresponding points on the true tracks. After the n -step track iteration, an association of the reconstructed track points to the points on the true tracks is established. The correction vectors point from the reconstructed track points to the points on the true tracks, and the distortion vectors from the points on the true tracks to the reconstructed track points.

By repeating the calculation with different numbers of track iteration steps, we found that three iteration steps were sufficient.

5.2 Boundary Condition

Independent of the E-field in the TPC, any ionization that happens at the anode would be reconstructed at the same position. Thus, in the displacement map, there is no spatial distortion at the anode.

The spatial displacements in the TPC are caused by the differences of the actual E-field the electrons drift in, and the E-field used in reconstruction. The reconstructed spatial position and the true spatial position are associated with each other by the position at the read-out planes with equivalent drifting time. The displacement vectors connect them directly without explicit knowledge of the position at the read-out planes. The spatial displacement vectors are related to the accumulated E-field distortion from the position of the ionization to the read-out planes. Ionized electrons which are produced at the anode are immediately read out with no time to be affected by E-field distortions.

As mentioned in Section 2.1, the coverage of the laser scans in MicroBooNE are restricted near the anode. The gap in between the anode and the edge of laser coverage is roughly 50 cm. Considering the main source of E-field distortion (space charge from cosmic and the detector geometry), we expect no rapid change in the E-field distribution. Thus we anticipate only small changes of spatial displacements with respect to the spatial coordinates.

We impose the boundary condition that the spatial displacement is null at the anode. With interpolation, the effective region of the displacement maps increases by about 20%. The validation of the displacement maps with the boundary condition included can be found in Section 5.5.

5.3 Interpolation

In order to obtain the spatial displacement vectors on the regular grid, we interpolate them from the ones associated with the track points. The regular grid points are located at the center of each bin in the spatial displacement maps. Each bin has the same size, about $10\text{ cm} \times 10\text{ cm} \times 10\text{ cm}$.

As mentioned in Section 2.1, laser beams do not reach the area blocked by the field-cage rings and the area near the anode. Given the bin size and the area of missing coverage, we expect

the E-field distortion only causes small variations in spatial displacement along the regular grid. Interpolation could provide a fair estimation of the spatial displacement in the low coverage area.

Interpolation is implemented in two steps. We first create a mesh of all the track points by using Delaunay triangulation. Then barycentric coordinates of the grid points in the corresponding Delaunay triangulation unit are computed, and they are further applied to achieve the spatial displacement vectors on the grid points.

The interpolation method is also used in the intermediate step of track iteration (Section 5.1.2). It is also applied in the calculation of drift velocity map and E-field map.

5.3.1 Mesh with Delaunay Triangulation

For the correction map, the mesh base is the collection of all the reconstructed track points. While for the distortion map, the mesh base is the collection of all the true track points which are the ends of the displacement vectors.

Three-dimensional Delaunay triangulation meshes a volume with tetrahedrons as unit elements. This guarantees that the whole volume of interest can be filled without gaps. The vertices of a unit tetrahedron are four reconstructed track points (true track points) for interpolating correction vectors (distortion vectors).

Delaunay triangulation has the property that the surrounding sphere of any unit tetrahedron must not contain any other mesh points. Thus, a unit tetrahedron usually has similar size as the surrounding units and its vertices are relatively close to each other with the given density of the mesh points. Therefore, the interpolated values are eligible to represent the local characteristics such as the spatial displacement. A diagram of a tetrahedron, a unit of the mesh in Delaunay triangulation, as shown in Figure 6.

We use *CGAL 3D triangulation* [14] [15] for meshing with Delaunay triangulation.

5.3.2 Barycentric Coordinates

Interpolation at a certain position \mathbf{P} uses the reference of the tetrahedron which accommodates \mathbf{P} . The barycentric coordinates system is the reference system that we use.

With the position information of four tetrahedron vertices $\mathbf{V}_1(x_1, y_1, z_1)$, $\mathbf{V}_2(x_2, y_2, z_2)$, $\mathbf{V}_3(x_3, y_3, z_3)$, $\mathbf{V}_4(x_4, y_4, z_4)$, the coordinates can be calculated,

$$\begin{pmatrix} \lambda_1 \\ \lambda_2 \\ \lambda_3 \end{pmatrix} = \mathbf{T}^{-1}(\mathbf{P} - \mathbf{V}_4),$$

\mathbf{P} is the position of interest for interpolation, \mathbf{T} is the matrix,

$$\mathbf{T} = \begin{pmatrix} x_1 - x_4 & x_2 - x_4 & x_3 - x_4 \\ y_1 - y_4 & y_2 - y_4 & y_3 - y_4 \\ z_1 - z_4 & z_2 - z_4 & z_3 - z_4 \end{pmatrix}$$

$\lambda_{1,2,3,4}$ are the barycentric coordinates of \mathbf{P} . The remaining λ_4 can be found by $\sum \lambda = 1$.

Effectively, $\lambda_{1,2,3,4}$ are the ratios of the tetrahedron volumes $\mathbf{P}\mathbf{V}_2\mathbf{V}_3\mathbf{V}_4$, $\mathbf{P}\mathbf{V}_1\mathbf{V}_3\mathbf{V}_4$, $\mathbf{P}\mathbf{V}_1\mathbf{V}_2\mathbf{V}_4$, $\mathbf{P}\mathbf{V}_1\mathbf{V}_2\mathbf{V}_3$, relative to the tetrahedron volume $\mathbf{V}_1\mathbf{V}_2\mathbf{V}_3\mathbf{V}_4$. This also applies when \mathbf{P} is located on the

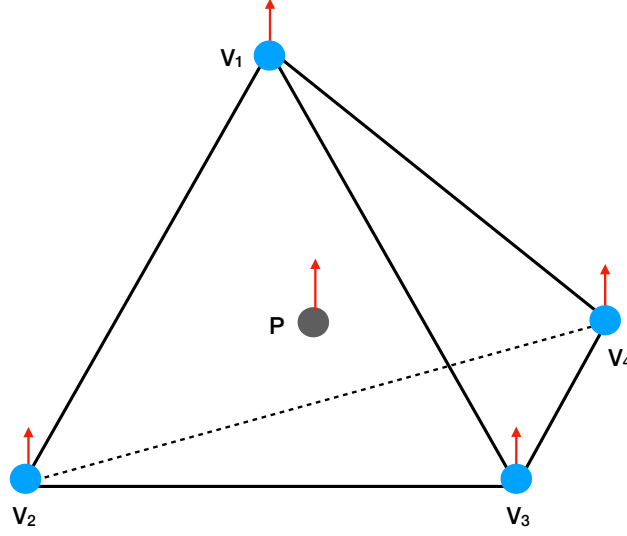


Figure 6. Diagram of a unit tetrahedron of the Delaunay Triangulation. In our application, such tetrahedrons are used as mesh units for interpolating physics quantities represented by vectors. The blue mesh points are the start of the mesh vectors and correspond to the reconstructed track points. The red arrows represent the correction vectors. The grey point **P** shows the position we aim to interpolate to.

surface or the edge or the vertex of the tetrahedron. The volumes $\mathbf{PV}_2\mathbf{V}_3\mathbf{V}_4$, $\mathbf{PV}_1\mathbf{V}_3\mathbf{V}_4$, $\mathbf{PV}_1\mathbf{V}_2\mathbf{V}_4$ and $\mathbf{PV}_1\mathbf{V}_2\mathbf{V}_3$ may be null.

Finally, the value at the position of interest Δr can be interpolated by

$$\Delta r = \sum_i \lambda_i \Delta r_i$$

Δr_i are the values at each vertex.

An example of interpolating the spatial displacement vector $\mathbf{d} = (dX, dY, dZ)$ is

$$dX = \lambda_1 dX_1 + \lambda_2 dX_2 + \lambda_3 dX_3 + \lambda_4 dX_4$$

$$dY = \lambda_1 dY_1 + \lambda_2 dY_2 + \lambda_3 dY_3 + \lambda_4 dY_4$$

$$dZ = \lambda_1 dZ_1 + \lambda_2 dZ_2 + \lambda_3 dZ_3 + \lambda_4 dZ_4$$

$\mathbf{d}_{1,2,3,4}(dX_{1,2,3,4}, dY_{1,2,3,4}, dZ_{1,2,3,4})$ are the spatial displacement vectors at the four vertices.

5.4 Sub-Map Merging and Statistical Uncertainty

Originally only the overall closest four track points determine a displacement map bin center. To increase data statistics and reduce bias from individual track points, we divide the original track set into m subsets. Then a given displacement map bin center is determined by four different track points for each of the m subsets.

With regard to each track, all m reconstructed track points are placed into the same subset. For example, the 1-st reconstructed track point of track **A1** together with the $(m + 1)$ -th, the $(2m + 1)$ -th

and so on are grouped to compose a new track $\mathbf{A1}_1$ for subset 1. In subset i , a new track $\mathbf{A1}_i$ contains the i -th, $(m + i)$ -th ... reconstructed point of the original track $\mathbf{A1}$. All the reconstructed points of $\mathbf{A1}$ can be found in the subsets and none of the reconstructed points appears in different subsets. Track $\mathbf{A1}_n$ (n can be any integer from 1 to m) shares the same true laser track as the one that corresponds to track $\mathbf{A1}$. The same procedure applies to every track in the original set. Every subset has the same number of tracks as the original one.

The track set division is done before the calculation of displacement vectors. Thus, in each subset, we still separate sample \mathbf{a} from the upstream laser sub-system and sample \mathbf{b} from the downstream laser sub-system. Each subset can produce a distortion map and a correction map which have similar coverage as the ones from the original track set. Therefore, with m subsets, we have m sub-distortion-maps and m sub-correction-maps.

With the interpolation procedure explained in Section 5.3, the displacement vector on a grid point only depends on the tetrahedron which encloses the grid point. This means that only four track points and their displacement vectors determine the representative displacement vector in a $10 \text{ cm} \times 10 \text{ cm} \times 10 \text{ cm}$ bin. Without subset division, the typical spacing in between track points is $\sim 3 \text{ mm}$ in reconstructed tracks. Hence, in a large area, the track points density is high and most of them do not contribute to the displacement map.

Considering the density of the track points, we divide the original track set into 50 subsets for both the simulated track set and the laser data track set. We then average the corresponding 50 sub-maps to issue a final map. The displacement vector on a grid point of the final map is the mean of 50 values at the same point from sub-maps. Therefore, the displacement vector on a grid point is calculated with the participation of up to 200 track points and their displacement vectors. It is unlikely that some individual track points with large bias could negatively affect the result on a grid point. The number of subsets is chosen to be 50, so that the statistics in each bin are large enough, while maintaining the shape and characteristics of the typical unit tetrahedron.

Due to small differences in the interpolation meshes of 50 subsets, the region with valid interpolated displacement may vary by a small amount at the edges. In each bin of the final map, the displacement vectors are the average of up to 50 displacement vectors from the sub-maps. Meanwhile, the standard deviation of the 50 X, Y, Z components from the displacement vectors are taken as the statistical uncertainty of the final map.

5.5 Bias Study and Systematic Uncertainty

With tracks generated through simulation, we calculate the displacement maps. The bias is defined as the difference of the simulation truth and the calculated displacement map from the simulated tracks.

The fact that small biases of the displacement maps from toy simulation are found, demonstrates the effectiveness of the methodology. The bias of the displacement maps from laser simulation is taken as systematic uncertainty for the displacement maps determined in data.

In the following, we use the distortion map as an example to explain the bias study by toy simulation and laser simulation. As stated earlier, the distortion map and the corresponding correction map show similar spatial displacement which can be converted to each other. For both the distortion map and the correction map, we use the same TPC boundary as described in Section 2.1, considering the cut-off in reconstruction. The bins with calculated displacement show

the rough coverage of the laser, which might be slightly smaller than the actual coverage due to the bin size. If the distortions of the E-field lead the ionizing electrons to be out of the TPC active volume from the edge, the displacement vector in the edge bins of both the distortion map and the correction map may be difficult to represent. In that case, the correction map would show a smaller area than the actual TPC active volume.

5.5.1 Bias Study by Toy Simulation

Figure 7 is the calculated distortion map by toy simulation at $Z = 518.00 \pm 5.18$ cm (central Z). From left to right, it shows the distortion components $dX = X_{\text{reco}} - X_{\text{true}}$, $dY = Y_{\text{reco}} - Y_{\text{true}}$, $dZ = Z_{\text{reco}} - Z_{\text{true}}$, which are the result of displacement calculation, boundary condition imposing and interpolation.

At central Z , dX has a maximum distortion towards the cathode at $X \approx 170$ cm of about ~ 4 cm. The maximum in dX is closer to the cathode because of space charge, which is the main contribution to the E-field distortion in MicroBooNE, accumulating along the drift direction. At the region closest to the anode and the cathode, dX is negligible. Yet, a distortion leads reconstructed Y to turn inwards when closer to the cathode, up to ~ 15 cm. dY is almost symmetric with respect to $Y = 0$. dZ is generally small and uniform.

Figure 8 shows the corresponding standard deviation of the calculated distortion in each bin at central Z (Section 5.4). In general, the standard deviations of dX , dY , dZ are found to be small. In comparison to other distortion components, the larger standard deviation in dZ implies that the calculation of the displacement vectors is affected by the track angle.

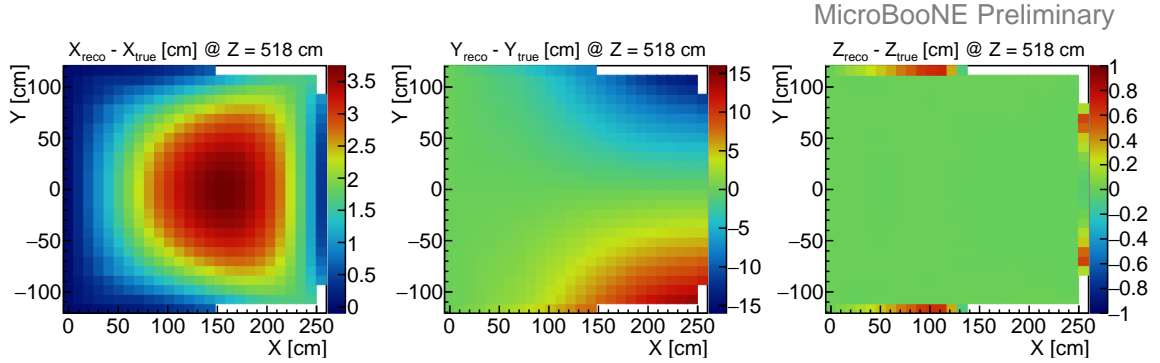


Figure 7. Calculated distortion map from a toy simulation showing a slice at central Z . All three components are shown: $dX = X_{\text{reco}} - X_{\text{true}}$ (left), $dY = Y_{\text{reco}} - Y_{\text{true}}$ (middle), $dZ = Z_{\text{reco}} - Z_{\text{true}}$ (right).

The difference of the simulation truth and the calculated distortion is taken as the bias of the algorithm excluding the reconstruction process. The bias $\Delta dX = dX_{\text{true}} - dX_{\text{calc}}$, $\Delta dY = dY_{\text{true}} - dY_{\text{calc}}$, $\Delta dZ = dZ_{\text{true}} - dZ_{\text{calc}}$ at central Z is displayed in Figure 9. We observe good agreement with small bias. The worse performance at the TPC edges is due to a combination of lack of track coverage and interpolation.

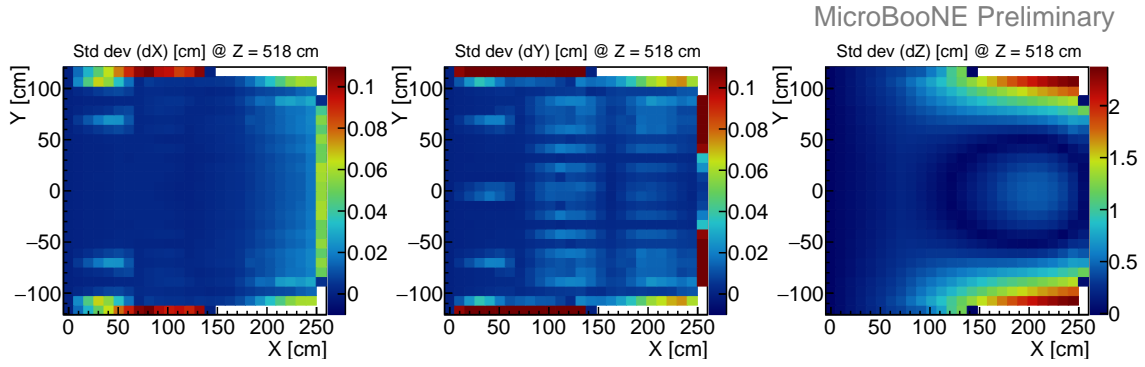


Figure 8. Standard deviation of the calculated distortion for dX , dY and dZ at a central Z slice in the toy simulation.

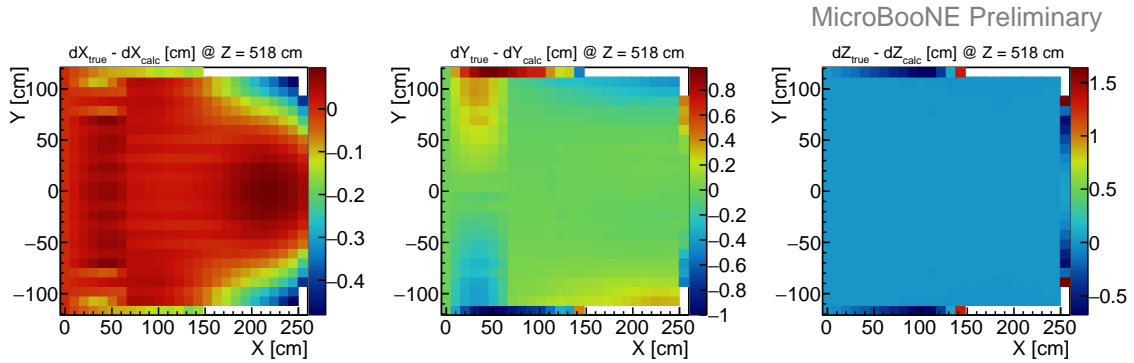


Figure 9. Bias in $\Delta dX = dX_{\text{true}} - dX_{\text{calc}}$, $\Delta dY = dY_{\text{true}} - dY_{\text{calc}}$, $\Delta dZ = dZ_{\text{true}} - dZ_{\text{calc}}$ from the toy simulation shown for a slice at central Z . In each bin the bias is relatively small compared to the distortion shown in Fig. 7.

5.5.2 Bias Study by Laser Simulation

The calculated distortion map determined by the laser simulation at a central Z slice is presented in dX , dY and dZ components in Figure 10. This distortion map is determined from the same E-field simulation, and thus input spatial distortion, as the one determined in the toy simulation study. For this central Z slice, the main features of the distortion are similar. Compared to Figure 7, the maximum distortions in dX and dY have very similar magnitude and similar position, while the coverage near the cathode and the TPC bottom are slightly different. A possible reason for the difference is the behaviour in reconstruction with more diffuse charge deposition.

Figure 11 illustrates the corresponding uncertainties in measured standard deviations in each bin at central Z . Comparing to the standard deviations of dX , dY , dZ from toy simulation, the ones from laser simulation fluctuate more, but in general they still remain reasonably small. The larger standard deviation in dZ (at central Z) at the TPC top and bottom close to the cathode, keeps the same scale as from toy simulation. This again implies the angle preferences of the calculation

as expected. We attribute this increase in statistical fluctuation of distortions to the reconstruction process.

The bias $\Delta dX = dX_{\text{true}} - dX_{\text{calc}}$, $\Delta dY = dY_{\text{true}} - dY_{\text{calc}}$ and $\Delta dZ = dZ_{\text{true}} - dZ_{\text{calc}}$ at central Z is shown in Figure 12. In comparison with the bias from toy simulation (Figure 9), the magnitudes of the bias slightly increase, but still are at the sub-centimetre level. The slightly asymmetrical distributions of ΔdY and ΔdZ in Figure 12 also suggest an asymmetry introduced by reconstruction.

The bias here is also taken as the systematic uncertainty of the displacement calculation.

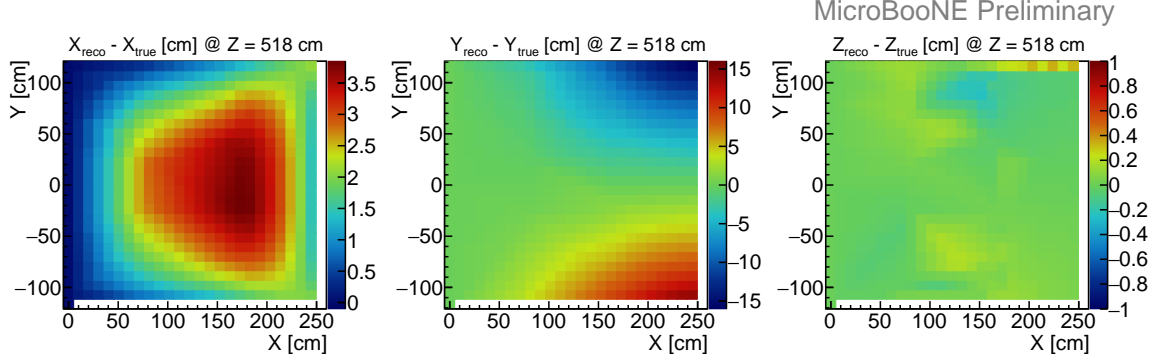


Figure 10. Calculated distortion map from the full laser simulation at a central Z slice. Shown is $dX = X_{\text{reco}} - X_{\text{true}}$ (left), $dY = Y_{\text{reco}} - Y_{\text{true}}$ (middle), $dZ = Z_{\text{reco}} - Z_{\text{true}}$ (right).

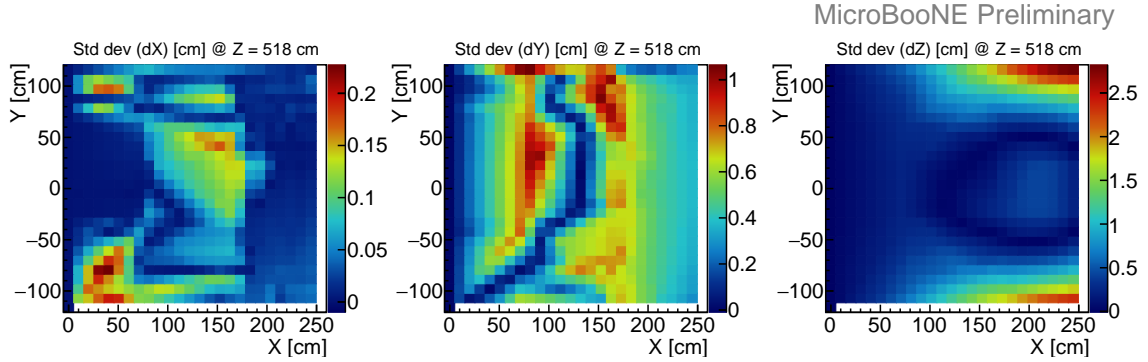


Figure 11. Standard deviation of the calculated distortion for dX , dY , dZ for a central slice in Z in the laser simulation.

5.5.3 Coverage of the TPC volume with the UV-laser method

The calculated distortion map by the laser simulation is generally very close to the true distortion map. Yet, at the edge of the TPC a sharp edge of calculated distortion from the centre of the X - Y to the top and bottom ends of the anode is noticeable in all views, as shown in Figure 13. Moreover, the bias of the same edge Z slice (Figure 14) shows a larger bias at the centre of the X - Y plane

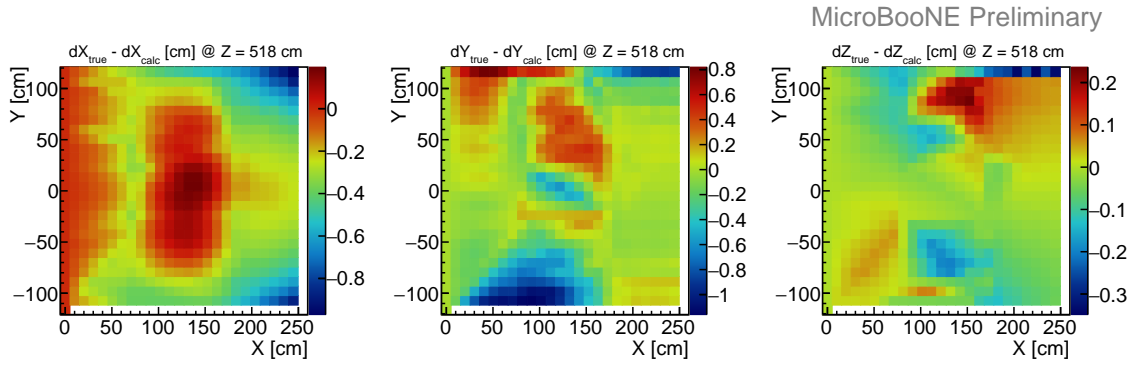


Figure 12. Bias as $\Delta dX = dX_{\text{true}} - dX_{\text{calc}}$, $\Delta dY = dY_{\text{true}} - dY_{\text{calc}}$, $\Delta dZ = dZ_{\text{true}} - dZ_{\text{calc}}$ from the full laser simulation at a central Z slice. This bias shows the overall effect of the distortion calculation, the track reconstruction and the selection. In most of the bins, the bias is relatively small compared to the distortion.

where the sharp edge is seen in Figure 13. This is due to the specific placement of the laser mirrors in MicroBooNE. The bias ΔdY are relatively large at lower Y and ΔdZ reaches ~ 10 cm.

Since cosmic ray muons are also used in MicroBooNE to determine the distortion map as a separate technique, we are able to fill in the regions where the UV-laser method has larger uncertainties. Thus we define a region of validity where the UV-laser techniques shows lowest uncertainty. As these regions are at the center of the TPC and the method using cosmic ray muons is expected to work better towards the edges, a combination is expected to improve the overall maps.

As in simulation the distortion is continuous by design; the sharp edge in reconstructed distortion is an artificial effect caused by the algorithm. The closest-point projection technique introduces an angular dependence in the initial determination of the displacement vectors. The track iteration does reduce this bias, but is less effective at the edge Z region, which is due to the placement of the mirrors and thus the start points of the laser tracks. Where these enter the TPC, they are close to collinear and pointing to the same spot on the mirror. In Figure 2 we show that the start points of the laser tracks are mostly located in the gap of tracks from the other side. Also, tracks which reach the other end in Z usually have small angle differences compared to all tracks. Imposing a boundary condition at the anode, together with interpolation, extends the local discontinuity from two points to a sharp triangle-like region in distortion.

Figure 15 and Figure 16 show the distortion and the bias determined by toy simulation at the same Z slice. The sharp triangle-like region, the large bias ΔdY close to the cathode at top and bottom Y edge and the large bias ΔdZ near the cathode are more pronounced.

We proceed to define a more limited region of validity of the displacement map based on the bias and resolution maps. Figure 17 shows the bias of the calculated distortion to the laser simulation truth in three components $\Delta dX = dX_{\text{true}} - dX_{\text{calc}}$, $\Delta dY = dY_{\text{true}} - dY_{\text{calc}}$, $\Delta dZ = dZ_{\text{true}} - dZ_{\text{calc}}$ in each bin. ΔdY has tails up to ± 5 cm, and distribution of ΔdZ has tails up to ± 10 cm. The bias ΔdX , ΔdY , ΔdZ derived by toy simulation are shown in Figure 18. The bias distributions are similar in Figure 17 and Figure 18. The difference is due to additional bias introduced by the reconstruction as determined in the laser simulation, where $d = \sqrt{dX^2 + dY^2 + dZ^2}$ is the length of the displacement

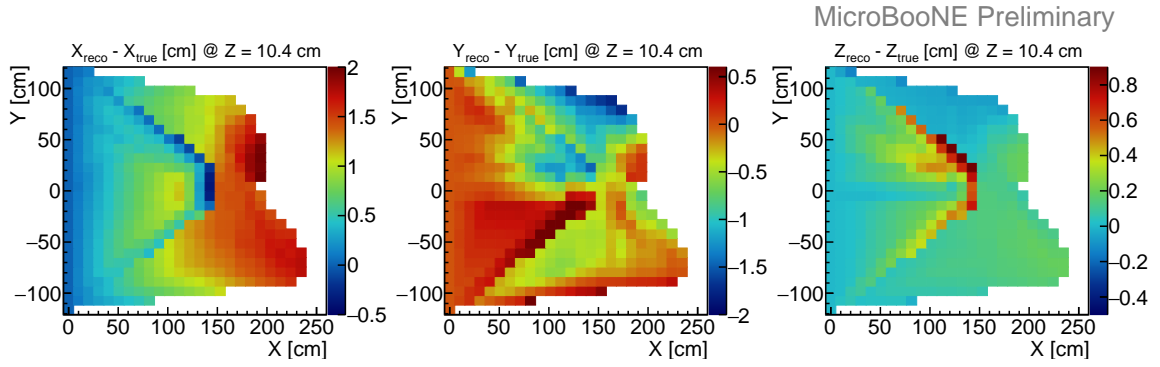


Figure 13. Calculated distortion map from the full laser simulation at an edge slice in Z . Shown are $dX = X_{\text{reco}} - X_{\text{true}}$ (left), $dY = Y_{\text{reco}} - Y_{\text{true}}$ (middle), $dZ = Z_{\text{reco}} - Z_{\text{true}}$ (right). The blank parts are where the laser does not have coverage. A distinctive pattern from the centre of this edge slice in Z to the top and bottom of the anode is noticeable in each component view.

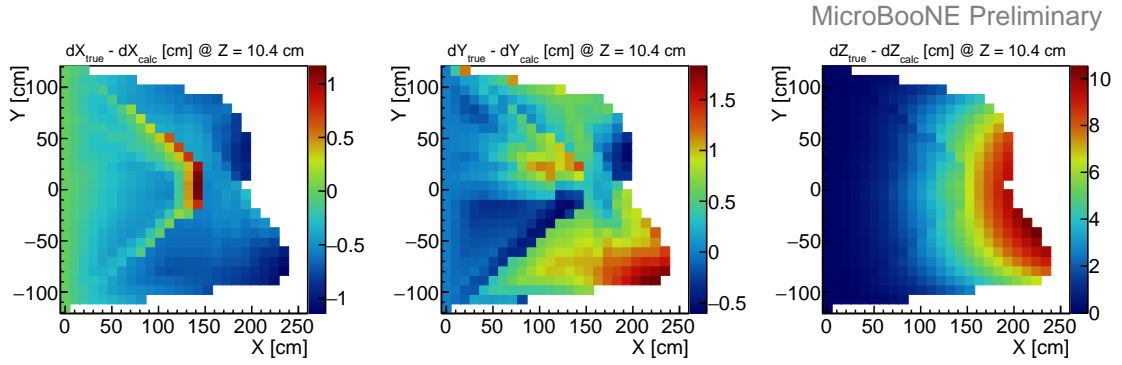


Figure 14. Bias of the calculated distortion from laser simulation at an edge slice in Z . Shows are $\Delta dX = dX_{\text{true}} - dX_{\text{reco}}$, $\Delta dY = dY_{\text{true}} - dY_{\text{reco}}$ and $\Delta dZ = dZ_{\text{true}} - dZ_{\text{reco}}$.

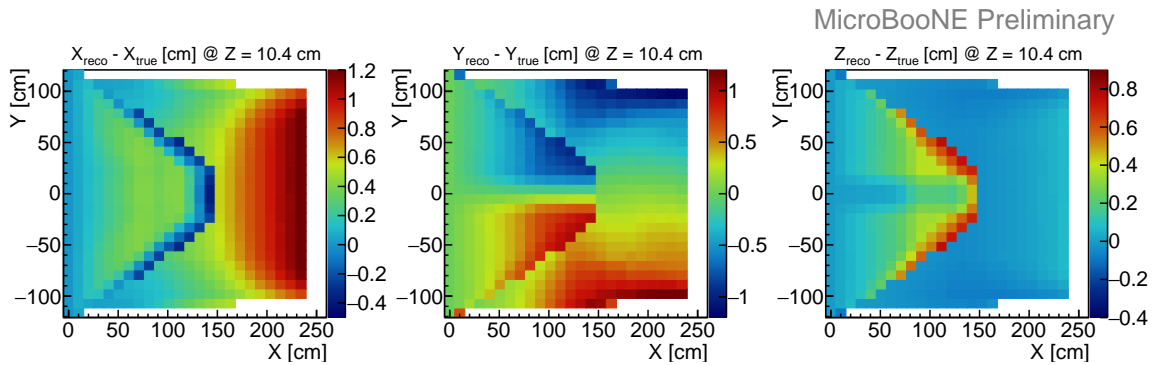


Figure 15. Calculated distortion map from toy simulation at an edge slice in Z . The distinctive pattern is more pronounced and in the same region as the one from the full laser simulation.

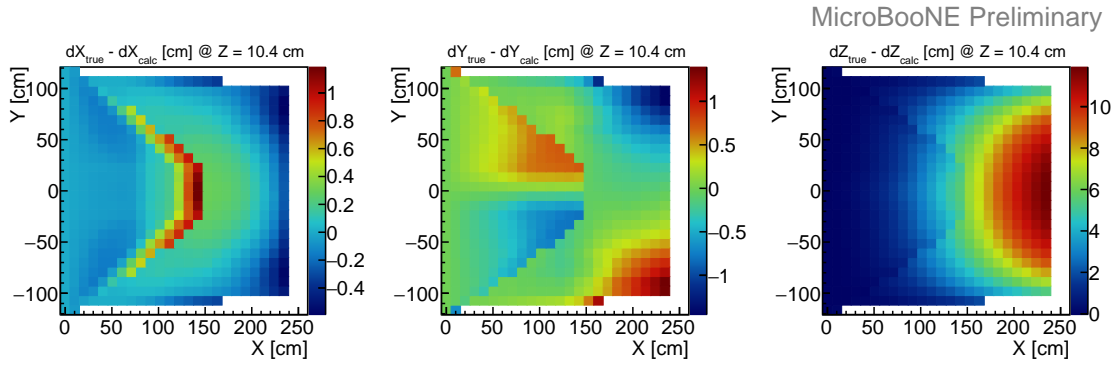


Figure 16. Bias of the calculated distortion from toy simulation at the edges in Z corresponds to the distortion maps shown in Figure 15.

vector. The full distribution of biases $\Delta d = d_{\text{true}} - d_{\text{calc}}$ determined by laser simulation in the whole TPC volume is shown in Figure 19. A noticeable population of d is positive because the calculation tends to underestimate d by the closest point projection initiated method.

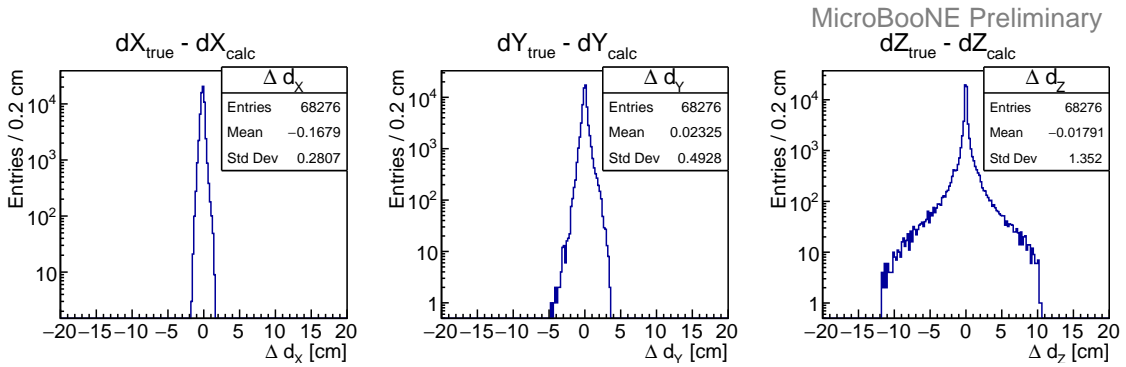


Figure 17. Histograms of the bias of the calculated distortions in three components ΔdX , ΔdY and ΔdZ from the laser simulation in the region with coverage. The bias distributions of ΔdY and ΔdZ are not symmetric with respect to the peak at 0.

Figure 20 displays the bias in dX , dY , dZ excluding the TPC edge at low Z ($0 \text{ cm} \leq Z \leq 46.8 \text{ cm}$) and high Z ($990 \text{ cm} \leq Z \leq 1036.8 \text{ cm}$). The bias in dY and dZ decreases in comparison to Figure 17. As expected, a noticeable amount of underestimated d are excluded when the valid region is limited to $46.8 \text{ cm} \leq Z \leq 990 \text{ cm}$.

Further constraint on Z to be between 99.8 cm and 937 cm results in a narrow bias of ΔdX , ΔdY and ΔdZ . The standard deviation of ΔdY and ΔdZ are 0.40 cm and 0.47 cm respectively, which is compatible with standard deviation of ΔdX (0.25 cm). The standard deviation of Δd is also down to 0.37 cm. The tails of these bias distributions typically end around $\pm 3 \text{ cm}$. More strict restriction of the region of validity do not significantly narrow the bias, so the final valid region is $99.8 \text{ cm} \leq Z \leq 937 \text{ cm}$ and the full length in X and Y .

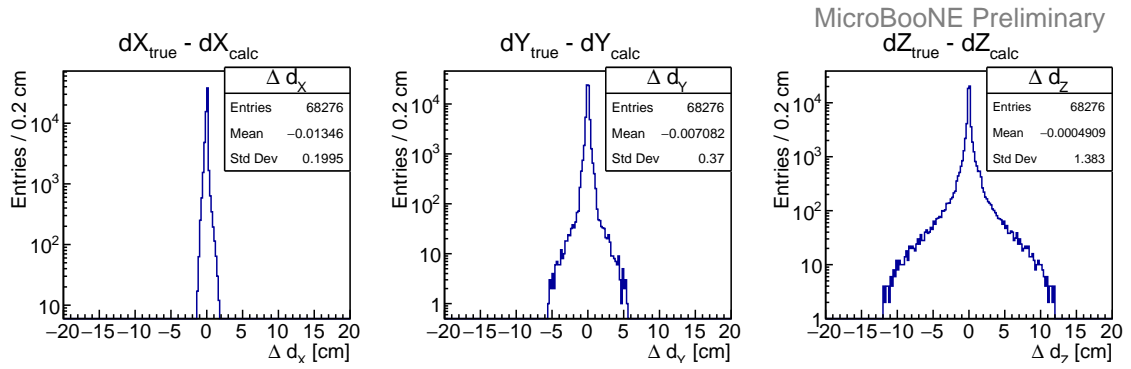


Figure 18. Histogram of the bias of the calculated distortions in three components ΔdX , ΔdY and ΔdZ from the toy simulation in the region with coverage. The bias distributions are symmetric around the peak at 0.

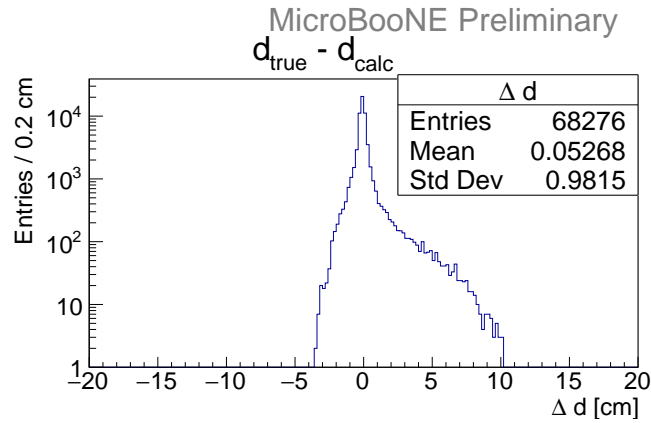


Figure 19. Histogram of the magnitude d of the distortion vector. $\Delta d = d_{\text{true}} - d_{\text{calc}}$ is the bias of the calculated distortion from the laser simulation of the map region with laser coverage. It is expected that overall the calculation distortion is smaller than the true distortion, because of the step of closest-point projection.

Validated by toy and laser simulations, the methodology for calculating displacement maps can be regarded as a reliable chain. Room for improvement lays in calculation of displacement vectors and laser track reconstruction.

6 E-field and Drift Velocity Maps

Although the E-field for drifting ionization electrons is designed to be uniform in between the cathode and the anode, this is difficult to reveal in practice. Both the TPC geometry and space charge effect can distort the E-field. To achieve better identification of charged particles and their locations in the TPC, a precise mapping of local E-field is necessary.

The E-field is calculated and then formed on a regular grid in the TPC active volume in true spatial coordinates on an adjustable regular grid. Here we set 26 bins along X , 26 bins along Y and

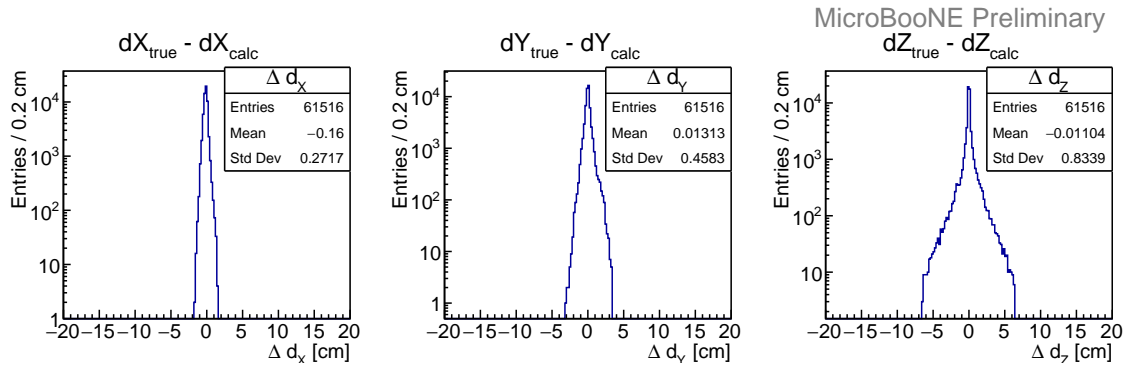


Figure 20. Histograms of the bias of the calculated distortion in three components ΔdX , ΔdY and ΔdZ from the laser simulation. If the region of $46.8 \text{ cm} \leq Z \leq 990 \text{ cm}$ is considered, the bias distributions are very close to null and symmetric. The spread of the bias distributions are also decreased compared to the ones including high Z and low Z ends.

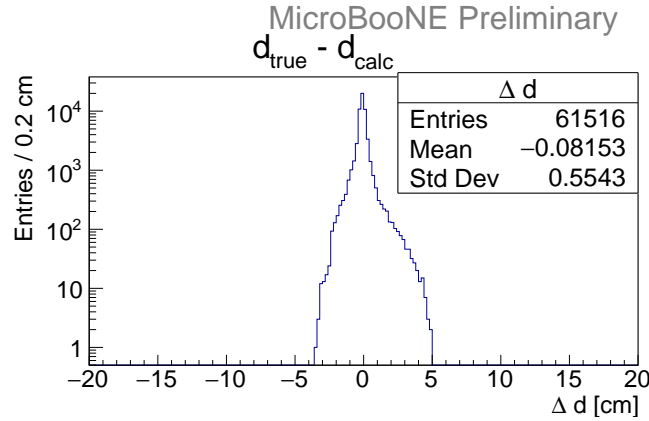


Figure 21. Histogram of the magnitude Δd of the bias of the calculated distortion from the laser simulation. The region of $46.8 \text{ cm} \leq Z \leq 990 \text{ cm}$ in TPC is considered, excluding high Z and low Z coverage. With this selection the tail of $\Delta d > 0$ is almost eliminated.

101 bins along Z and TPC edge is at the center of the edge-most bins. With further interpolation, the E-field can be determined at any position in the valid map area.

In the following, the method of how the E-field is extracted from distortions maps derived on UV-laser data is described. In principle it could be applied on any data source more generally.

6.1 Field lines

The direction of the E-field lines extend from the anode to the cathode. Ionizing electrons generated anywhere along a field line, drift to the same position at the anode. Since they share the same read-out position, they would be reconstructed along a line which passes that read-out position and is perpendicular to the anode plane.

We take the correction map which has a regular grid in reconstructed spatial coordinates as

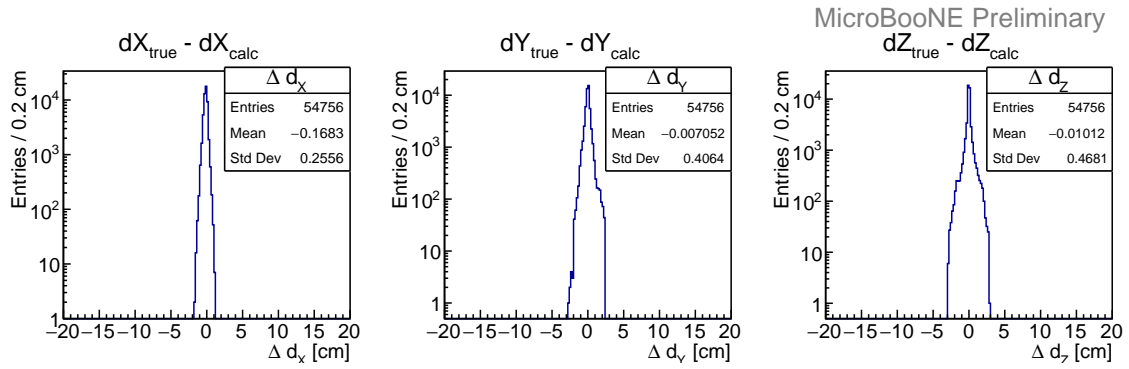


Figure 22. Bias of the calculated distortion in the three components ΔdX , ΔdY and ΔdZ from laser simulation. Only the region of $99.8 \text{ cm} \leq Z \leq 937 \text{ cm}$ is included. The bias distributions are now close to symmetric around the peak at 0. The standard deviation of ΔdX is ~ 0.2 , $\Delta dY \sim 0.4$, and $\Delta dZ \sim 0.4$.

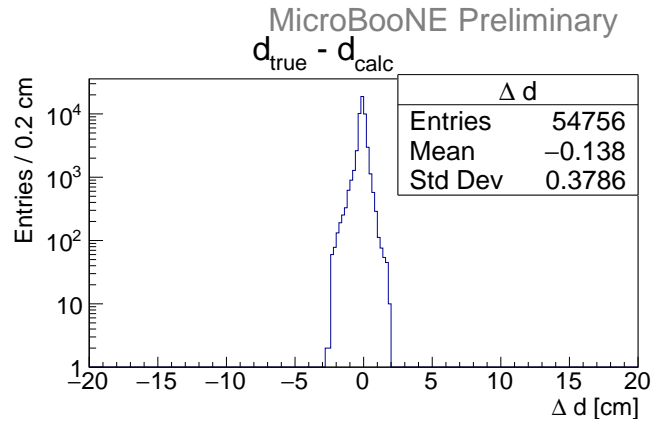


Figure 23. Histogram of the magnitude Δd of the bias of the calculated distortion from laser simulation, with $99.8 \text{ cm} \leq Z \leq 937 \text{ cm}$. Δd here is relatively small in each bin which has been considered. The standard deviation is $\Delta d \sim 0.4 \text{ cm}$.

the input of the E-field calculation. In Figure 24, the gray dots are the regular grid points in reconstructed spatial coordinates. The ones along the dashed line all correspond to the same read-out position (orange). The red arrows are the correction vectors on those gray grid points, so the turquoise dots are the corresponding true positions. We line up the turquoise dots by the distance of their corresponding reconstructed grid points to their read-out position. The connection from that read-out position to the first green dot, represents the field line in this step. Similarly, the continuous connection from a turquoise dot to the next turquoise dot forms the field line.

Figure 25 shows the field lines derived from laser data at central Y and at central Z . They are mostly smooth, and no crossing lines are observed. The distortion in the direction of the E-field is pronounced at central Z . Close to the cathode, the E-field bends outwards. Thus, in reconstructed spatial coordinates, the corner near the cathode at the top and the bottom edge is not seen. The gray boxes in Figure 25 indicate the projection of TPC active volume. In principle, the field lines should

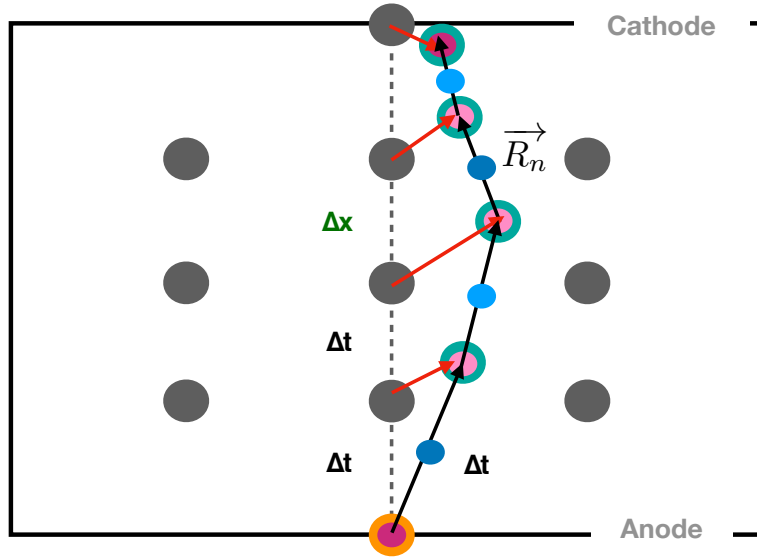


Figure 24. Diagram showing how the E-field is calculated. The gray dots are the regular grid points in reconstructed spatial coordinates. They are spaced by $\Delta x = v_0 \Delta t$, corresponding to Δt with the nominal drift velocity v_0 . The turquoise points are the positions of the actual energy deposition in true spatial coordinates. As the time sampling of the TPC is given, these are also spaced by Δt . The red arrows represent the correction vector pointing from the reconstructed to the corresponding true positions. Ionization electrons drifting from any turquoise dots along a field line would be read out at same orange point at the anode. Thus the line connecting these points, with \vec{R}_n the spatial vector at each step, follows the E-field. The black arrows indicate the direction of such derived E-field.

be contained in the TPC active volume. The top two field lines at central Z (bottom plot) exceed the gray box by ~ 1 cm. The E-field exists outside the TPC active volume around the boundaries, because the field-cage rings are still a few centimetres away from the active (instrumented by wires) volume boundaries. The E-field around the field-cage rings is typically stronger. It is not excluded that this effect is physical, but the uncertainties in this region are also compatible with 1 cm. Also, the field lines slightly exceed the gray box along the X direction. We obtain X coordinates via the nominal drift velocity along X in the TPC. The nominal drift velocity (v_0) is $1.098 \text{ mm } \mu\text{s}^{-1}$. We take the cathode position at 254.8 cm from an estimate of TPC drift length in MicroBooNE at a LAr temperature of (89 K). This value has an uncertainty of about 1 cm along X .

Some field lines in Figure 25 do not extend across the entire drift length due to a lack of laser coverage. The asymmetry in Z (upstream and downstream) may be due to the difference in the two laser positions and pulse energy settings. While the asymmetry in Y is mostly due to the fact that the dichroic mirrors have decreasing reflectance efficiency for larger incident angle.

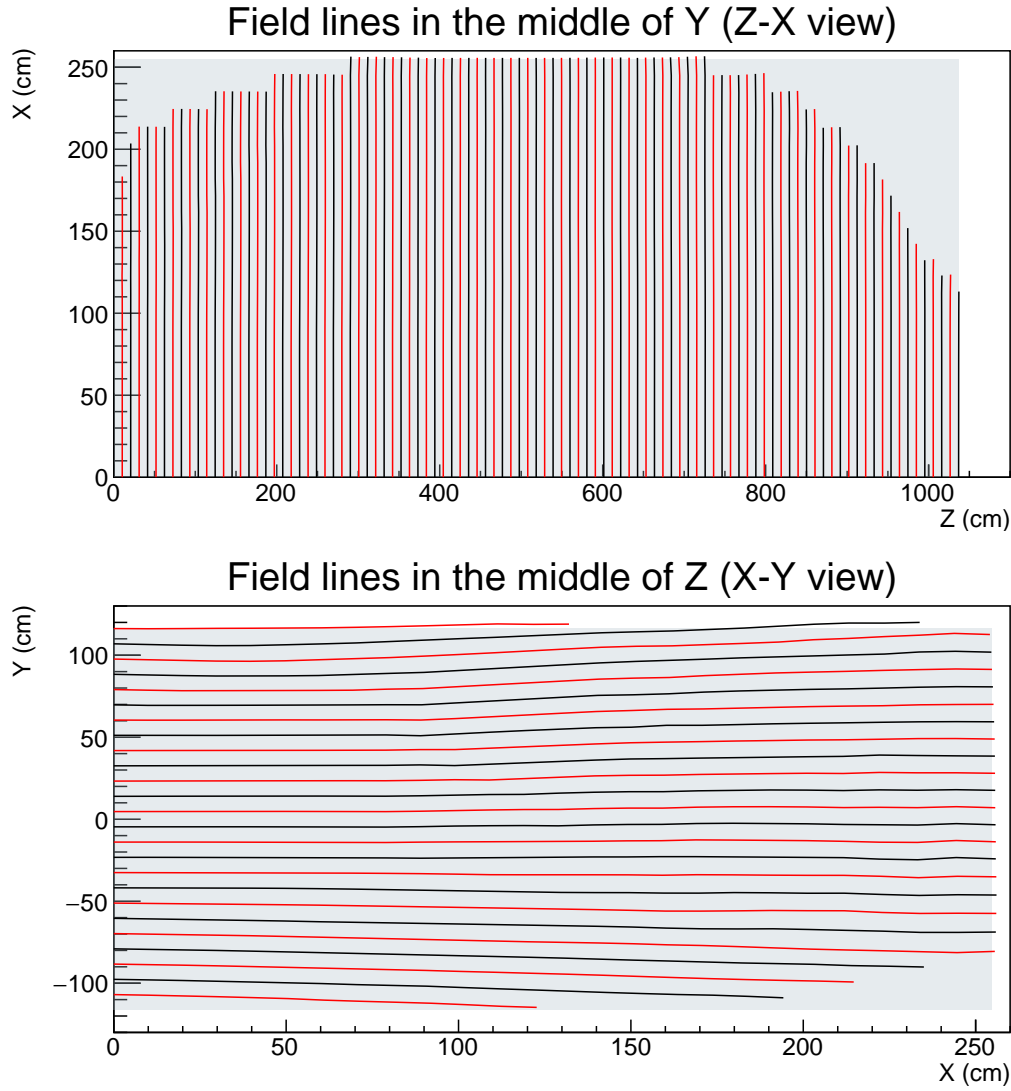


Figure 25. The upper plot shows the projection of the field lines at a central slice in Y , and the bottom plot shows the projection of field lines at central Z . The field lines are derived from laser data. Different line colors are used to distinguish neighbouring field lines. The gray box shows the projection of the TPC active area in true spatial coordinates.

6.2 Extraction of the Local Drift Velocity

We illustrate the calculation of the local drift velocity using Figure 24. We define a step as going from the read-out position to the first true track point position, or from one track point to the next in true coordinates. Ionizing electrons from the first true track point drift to the anode plane and thus readout position in a time Δt . The reconstruction procedure restores the position to a first point assuming a uniform E-field perpendicular to the readout plane at a distance $X_1 = |v_0| \cdot \Delta t$. All the reconstructed track points are spaced by $\Delta X = |v_0| \cdot \Delta t$ from each other, since they are on a regular grid in reconstructed spatial coordinates. The nominal drift velocity v_0 is taken as constant along

X , so the time difference from any gray point to the next gray point is also Δt . The n -th track point in reconstructed coordinates is associated to the n -th true point, where n is an integer between 1 and 24 for the grid used here. The time which is used in reconstruction of the n -th point is $n\Delta t$, so the drifting time from the n -th point to the readout point is also $n\Delta t$. Similarly, the time associated to the $(n + 1)$ -th reconstructed or true points is $(n + 1)\Delta t$. Therefore, the time of any step n is Δt , which is the same as the time in between two neighbouring gray points along X .

We regard the local drift velocity as constant during each step. The step vector \vec{R}_n is pointing from the n -th true point to the $(n + 1)$ -th. Eq. 6.1 shows the relation of $|\vec{R}_n|$ and ΔX .

$$\frac{|\vec{R}_n|}{\Delta X} = \frac{|\vec{v}_n|\Delta t}{|\vec{v}_0|\Delta t} \quad (6.1)$$

Thus, the local drift velocity can be calculated by Eq. 6.2.

$$|\vec{v}_n| = \frac{|\vec{R}_n|}{\Delta X} |\vec{v}_0| \quad (6.2)$$

The local drift velocity \vec{v}_n has the opposite direction of \vec{R}_n . We assign \vec{v}_n to the centre of step n .

If the correction vector on the n th reconstructed point is falsely calculated, it only affects \vec{R}_n and \vec{R}_{n+1} . Thus only the local drift velocity \vec{v}_n and \vec{v}_{n+1} are influenced.

If there is no spatial displacement, any local drift velocity \vec{v}_n would be the same as the nominal drift velocity \vec{v}_0 . If the correction vectors on the reconstructed points are ideal, the magnitude of the assumed nominal drift velocity $|\vec{v}_0|$ is irrelevant for the measurement of the velocity map. Any deviation would be absorbed by the correction map and the step vector \vec{R}_n would remain unchanged. The local drift velocity $|\vec{v}_n| = \frac{|\vec{R}_n|}{\Delta t} = \frac{|\vec{R}_n|}{\Delta X} |\vec{v}_0| = \frac{|\vec{R}_n|}{\Delta X} |\vec{v}_0|$ would also not change. However, the displacement vectors calculated as described in Section 5.1 contain angular dependence on the laser tracks. Thus, the magnitude of the nominal drift velocity $|\vec{v}_0|$ can be relevant.

The local drift velocity vectors on the regular grid are then interpolated from the drift velocities of the local steps. The interpolation procedure is described in Section 5.3.

6.3 Extraction of the Local E-field

The local E-field is derived from the local drift velocity map. The direction of the E-field is the same as the step vector \vec{R}_n . The magnitude of local E-field is determined from the corresponding local drift velocity by using the relation shown in Figure 26. The drift speed increases from $\sim 0.20 \text{ mm } \mu\text{s}^{-1}$ to $\sim 1.75 \text{ mm } \mu\text{s}^{-1}$ when the corresponding E-field increases from $\sim 0.02 \text{ kV cm}^{-1}$ to $\sim 0.66 \text{ kV cm}^{-1}$. This drift speed as function of E-field is taken from the LArSoft package and from references [16] and [17]. The drift speed as a parametric function of the E-field and LAr temperature is given in [17]. The LAr temperature is stably maintained at 89 K in MicroBooNE.

The drift speed has a non-linear, monotonic dependence on the E-field. Thus one can determine the local E-field from the measured local drift speed in magnitude and direction. We then use bisection to numerically trace down the magnitude of the local E-field. When the distortion of E-field is not dramatic, the change of drift speed is nearly linear around the nominal field $|\vec{E}_0| = 0.274 \text{ kV cm}^{-1}$.

We assign the local E-field vectors to the centre of the steps (blue points) shown in Figure 24. They share the same positions as local drift velocities of the steps. We also set the average E-field

of two neighbouring steps to the joint of those two steps (pink points). The start of the first step and the end of the last step are attached with the local E-field of the first and last step. The local E-field on the regular grid is formed by interpolation described in Section 5.3. We increase the mesh coverage of the interpolation near the anode and the cathode, and we enhance mesh density in the TPC as well.

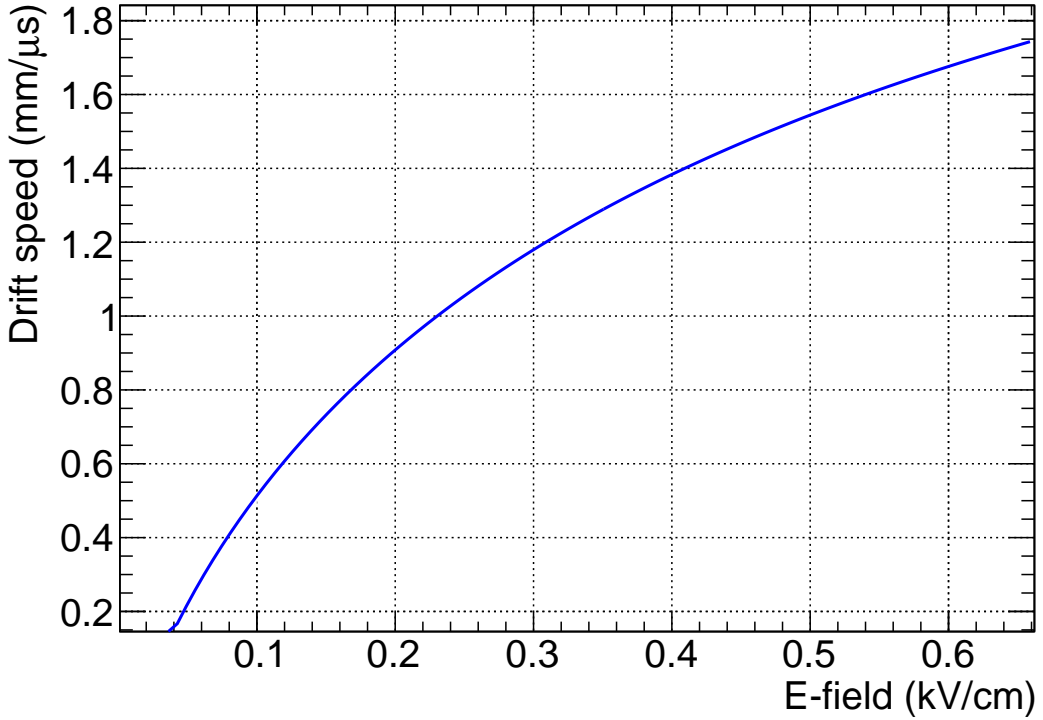


Figure 26. Drift speed as a function of E-field [16] and [17]. The range of E-field shown goes from 0.04 kV cm^{-1} to 0.66 kV cm^{-1} .

6.4 Validation of the E-field determination

The space charge simulation in LArSoft described in Section 4 contains an E-field map, a correction map and a distortion map. We take the correction map from the space charge simulation to calculate a E-field map. The calculated E-field map is compared to the simulation truth, which is the E-field map determined from the space charge simulation to validate the method of E-field calculation including the drift velocity calculation. The bias is defined as the bin to bin difference of calculated E-field and E-field from the simulation truth. It also folds uncertainties of the correspondence of the E-field map and the correction map in the space charge simulation. The E-field map of space charge we used has 21 bins in X , 21 bins in Y and 81 bins in Z . The first and last bin centres of each direction locate at the TPC limits. To avoid introducing different bias, we use the same binning for the calculated E-field map in validation.

Figures 27 and 28 show the calculated E-field (up) and the E-field of simulation truth (down) in central Z and edge Z respectively. We present 2D slices of the E-field map by the relative E-field distortion in percentage with respect to the nominal E-field $E_0 = 274$ V/cm in components, $(E_X - E_0)/E_0[\%]$ (left), $E_Y/E_0[\%]$ (middle), $E_Z/E_0[\%]$ (right). At central Z , near the cathode E_X is larger than E_0 by about 9%, and near the anode E_X is smaller than E_0 by about 6%. At central Z , E_Y is about 15% of E_0 and points outwards at the top and the bottom of the TPC. At central Z , E_Z is relatively small. The E-field distortion in Z direction is less than 1% of E_0 . At the edges in Z , near the cathode, E_X exceeds E_0 by about 1.5% and near the anode E_X is below E_0 by about 1%. The vertical component E_Y is about 4% of E_0 and points outwards at the top and the bottom of the TPC. The component along the beam E_Z points to the outside of the TPC. The maximum distortion in E_Z is about 10% of E_0 and the position of the maximum is at $X \sim 160$ cm and $Y \sim 0$ cm. The general shape of the calculated E-field distortion agrees well with simulation truth. The small coverage problem in the bins at the anode and the cathode is because the correction map of simulation truth does not correct spatial coordinates to those region in true spatial coordinates.

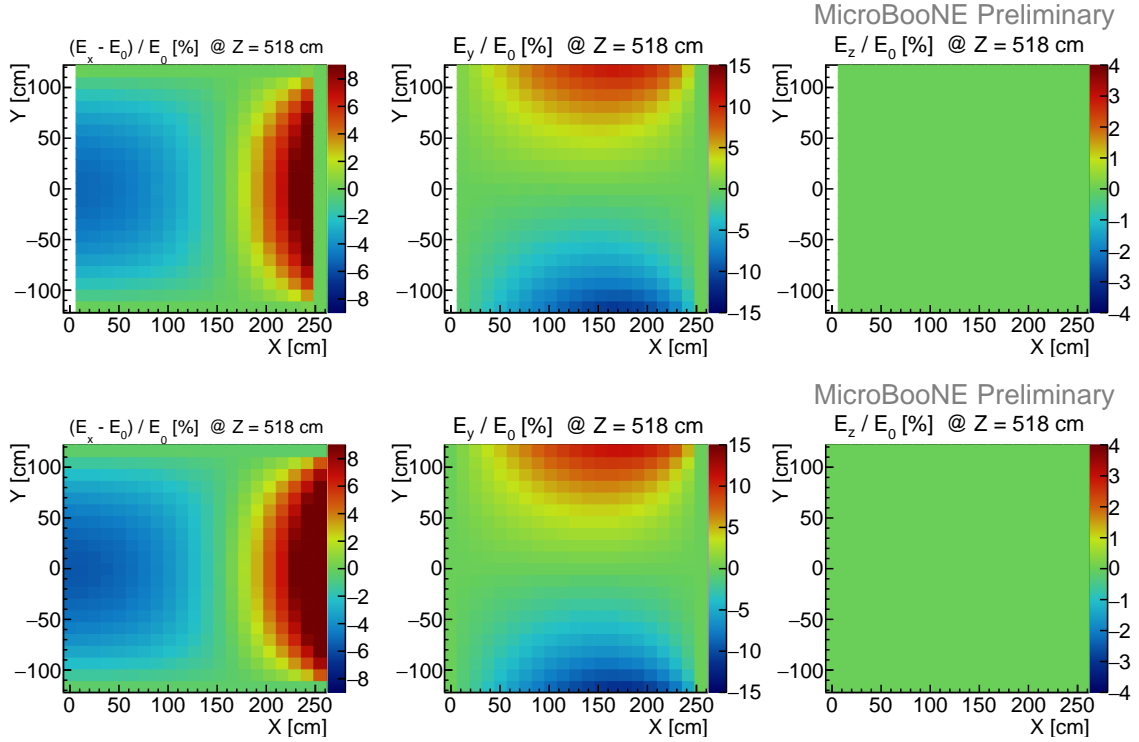


Figure 27. Relative E-field distortions (in percent) with respect to the nominal E-field in components $(E_X - E_0)/E_0[\%]$ (left), $E_Y/E_0[\%]$ (middle) and $E_Z/E_0[\%]$ (right). The upper row shows the result of the calculated E-field from the correction map based on a space charge simulation. The lower row shows the E-field of the space charge simulation [18], which is used as simulation truth here. Both of them are showing the E-field distortion at central slice in Z in the TPC true spatial coordinates.

Figure 29 shows the absolute bias of the calculated E-field and the input E-field in the simulation in V cm^{-1} . The distribution of X , Y and Z components of the bias are displayed. These distributions all narrowly peaked around null. The bias of E_X has a mean value of 0.35 V cm^{-1} and the standard

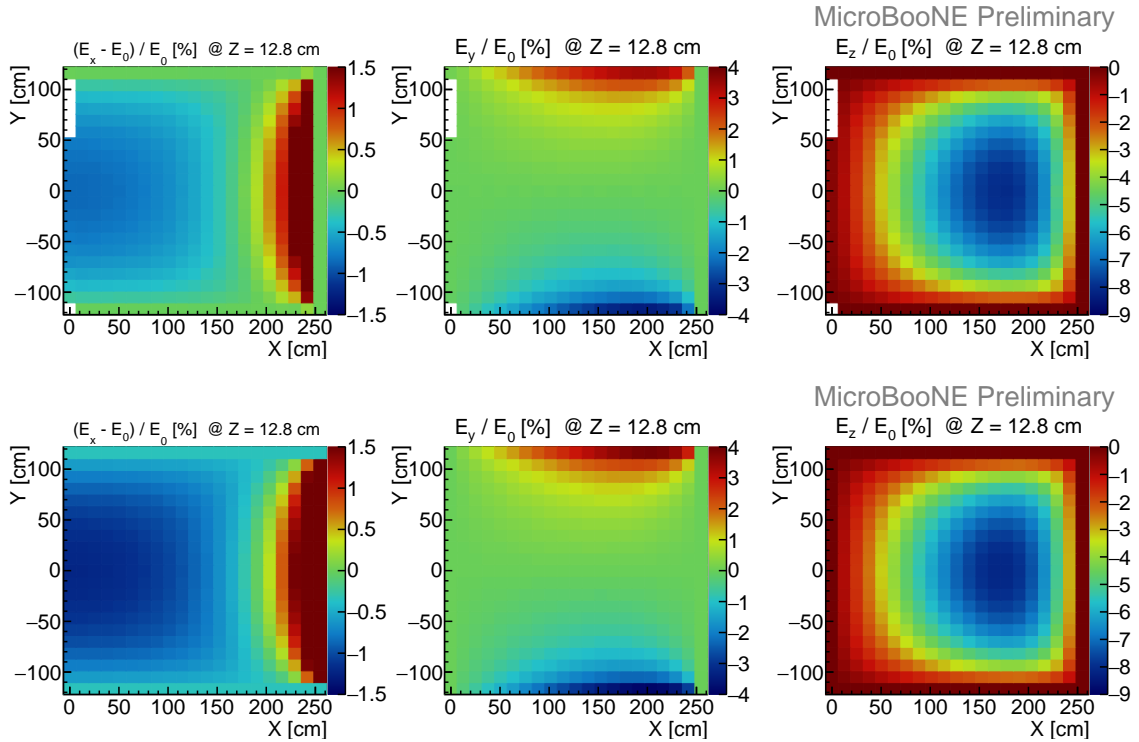


Figure 28. Relative E-field distortion (in percent) with respect to the nominal E-field in components $(E_X - E_0)/E_0[\%]$ (left), $E_Y/E_0[\%]$ (middle), $E_Z/E_0[\%]$ (right). The upper row is the result of the calculated E-field from the correction map based on a space charge simulation. The lower row is the E-field of the space charge simulation [18], which is used as simulation truth here. Both of them are showing the E-field distortion at an edge slice in Z in the TPC true spatial coordinates.

deviation of the bias in X , Y and Z components are 0.074 V cm^{-1} , 0.166 V cm^{-1} and 0.053 V cm^{-1} , respectively. Figure 30 shows the absolute bias of the magnitude of the E-field in V cm^{-1} . The mean and the standard deviation of the bias distribution are 0.35 V cm^{-1} and 0.074 V cm^{-1} respectively. The bias in E-field magnitude is dominated by the bias in X . The small bias is also visible in Figure 27 and 28. This may be caused by our limited knowledge of the cold cathode position. Overall, the bias between the reconstructed and simulated E-fields is negligible, which validates the method of calculating E-field and drift velocity.

7 Measurements in MicroBooNE

Using laser data collected with the MicroBooNE experiment and the track reconstruction and selection described in Section 3 we extract the spatial distortion and correction map, and their corresponding drift velocity and E-field maps.

7.1 Distortion Maps

With the method described in section 5 we derive the distortion and correction maps determined from UV-laser data. We present 2D slices of the 3D maps and the corresponding uncertainties.

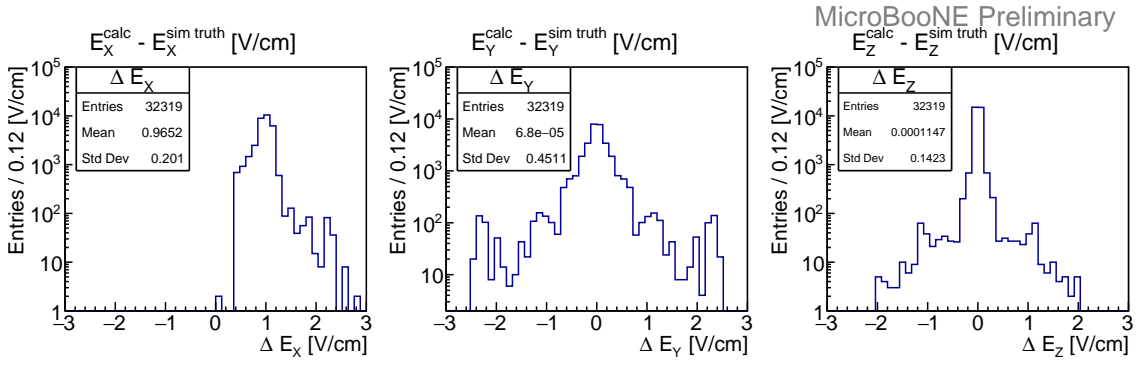


Figure 29. Distributions of bias components $E_X^{\text{calc}} - E_X^{\text{sim truth}}$, $E_Y^{\text{calc}} - E_Y^{\text{sim truth}}$ and $E_Z^{\text{calc}} - E_Z^{\text{sim truth}}$ in V cm^{-1} . Each entry of the distribution corresponds to the bias in one bin. The three bias distributions are narrowly peaked around 0.

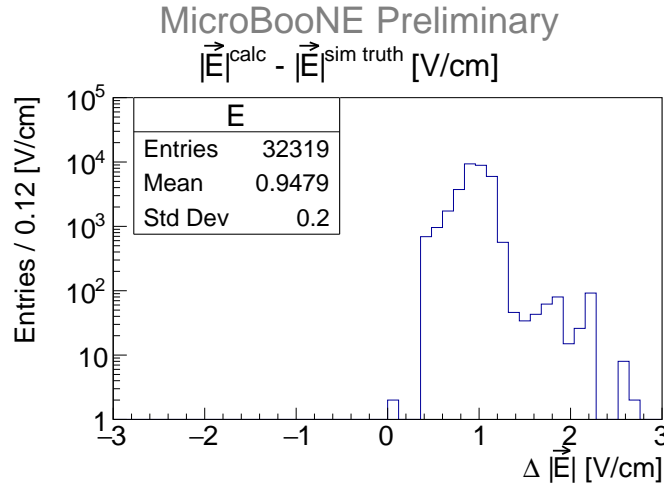


Figure 30. Bias distributions of the local E-field magnitude $|\vec{E}|^{\text{calc}} - |\vec{E}|^{\text{sim truth}}$ in V cm^{-1} . Each entry of the distribution is the bias in one bin. The calculated E-field is very close to the simulated truth within 0.5 V cm^{-1} .

Figure 31 shows at central Z the spatial distortion of dX , dY and dZ calculated from laser data. The corresponding figures from simulation are Fig. 7 and Fig. 10. The maximal dX observed in data is about 4 cm, positioning around $X \approx 160 \text{ cm}$ and $Y \approx 0 \text{ cm}$. It is larger than prediction and beyond the assessed uncertainty, which indicates that the build up of space charge in the simulation may be underestimated. Close to the cathode, the upper and lower edge of Y are distorted about 15 cm inwards in the TPC. dZ is relatively small and uniform. The overall shape of the spatial distortion is not very different from the one expected in simulation.

The standard deviation in each bin is calculated from 50 sub-maps. The corresponding central Z slice of the standard deviation is shown in Figure 32. Comparing to Figure 11, it does not increase significantly compared to the standard deviation in the laser simulation. This is taken as statistical uncertainty for spatial distortion in each bin. While the systematic uncertainty is estimated by the

Position (X, Y, Z) [cm]	$dX \pm \text{stat.} \pm \text{syst.}$ [cm]	$dY \pm \text{stat.} \pm \text{syst.}$ [cm]	$dZ \pm \text{stat.} \pm \text{syst.}$ [cm]
(174.11, -4.65, 518.40)	$4.22 \pm 0.34 \pm 0.10$	$-2.00 \pm 0.26 \pm 0.60$	$-0.01 \pm 0.44 \pm 0.11$
(30.72, -4.65, 518.40)	$1.15 \pm 0.02 \pm 0.05$	$-0.02 \pm 0.52 \pm 0.04$	$-0.01 \pm 0.06 \pm 0.01$
(225.32, -60.45, 518.40)	$1.11 \pm 0.58 \pm 0.37$	$6.51 \pm 1.04 \pm 0.05$	$0.09 \pm 0.68 \pm 0.14$
(225.32, 60.45, 518.40)	$1.46 \pm 0.38 \pm 0.38$	$-8.20 \pm 0.82 \pm 0.06$	$-0.01 \pm 0.48 \pm 0.05$

Table 2. Spatial distortion measured from laser data for selected representative points in the TPC.

bias of the true and calculated displacement in the laser simulation (Figure 12).

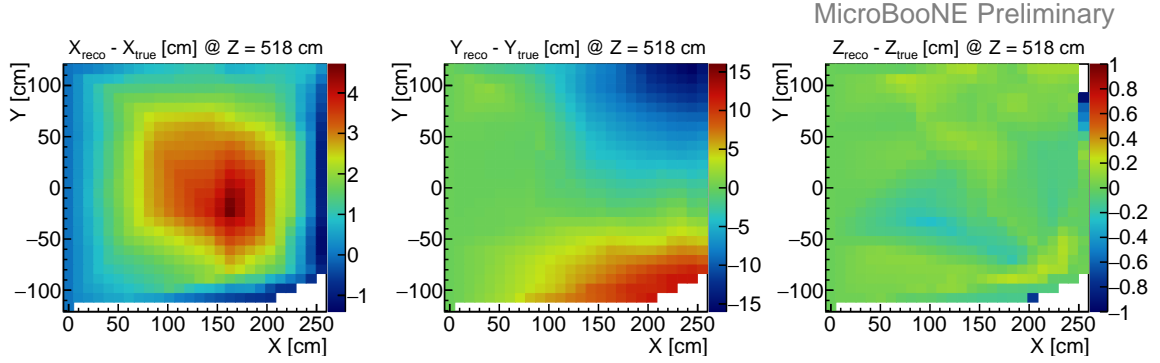


Figure 31. Calculated distortion map from laser data at a central slice in Z. Shown are the three components $dX = X_{\text{reco}} - X_{\text{true}}$ (left), $dY = Y_{\text{reco}} - Y_{\text{true}}$ (middle), $dZ = Z_{\text{reco}} - Z_{\text{true}}$ (right). In this Z slice the maximum dX is around 4 cm and the maximum dY is about ± 15 cm. The corresponding figures from simulation are Fig. 7 and Fig. 10.

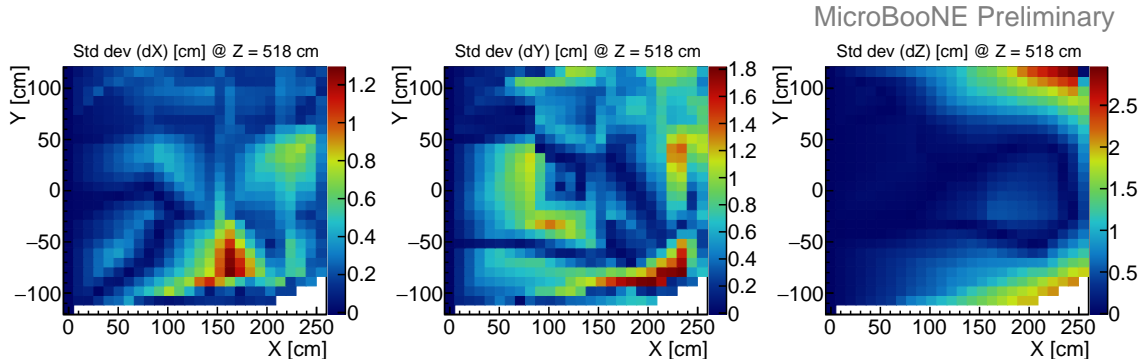


Figure 32. Standard deviations of the spatial distortion dX , dY , dZ corresponding to Fig. 31.

Selected spatial distortion values with their uncertainties are listed in Table 2.

Given the scale of the spatial distortions, in order to achieve more accurate tracking as well as calorimetric information from the TPC, it is crucial to correct such spatial distortions.

7.2 Drift velocity Map from Laser Data

The local drift velocity is calculated from the correction map based on laser data and then used to form a drift velocity map as described in section 6.2.

Figure 33 shows the drift velocity components with respect to the nominal drift velocity v_0 . In MicroBooNE, v_0 is $1.098 \text{ mm } \mu\text{s}^{-1}$. The nominal drift velocity is estimated by looking at the end of cathode piercing tracks and measuring the drift time of the ionization electrons to travel to the anode. Uncertainty on v_0 comes from the determination of the cold cathode position and the residual space charge effect at the cathode.

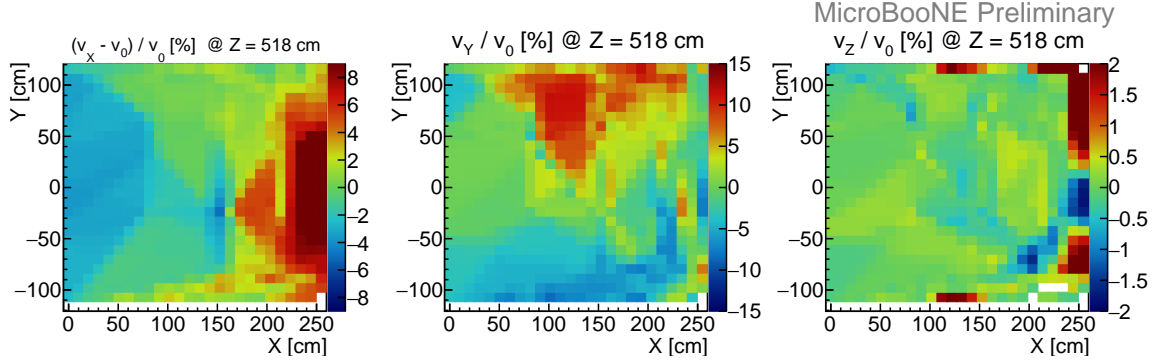


Figure 33. Relative drift velocity components (in percent) for the three coordinates $(v_X - v_0)/v_0$ [%] (left), v_Y/v_0 [%] (middle) and v_Z/v_0 [%] (right) at a central slice in Z . The drift velocity has a maximal distortion from the nominal drift velocity v_0 of about 10%.

At central Z , the drift velocity component along X is about 10% larger than v_0 near the cathode and v_X is about 6% smaller than v_0 near the anode. The area with larger v_X is slightly smaller than the area with smaller v_X . In the upper and lower region, v_Y is about $0.1 \text{ mm } \mu\text{s}^{-1}$ pointing outwards. The vertical drift velocity v_Z is relatively small and uniform at central Z .

The statistical uncertainty of the drift velocity is derived by error propagation from the correction map. Corresponding to each bin of the correction map, 500 correction vectors are generated according to a normal distribution with μ the central value of the correction vector and σ the standard deviation. We obtain 500 correction maps with reasonable statistical uncertainty in this way. We then propagate these 500 correction maps into velocity maps and in each bin we obtain 500 velocity components. We take the standard deviation from a fit to the distributions in every bin as the statistical uncertainty of the velocity measurement. As we are eventually interested in the E-field, more details on the uncertainties are given in section 6.3.

The systematic uncertainty of the local drift velocity is again determined by the bias study using the laser simulation. The bias is the difference of the calculated drift velocity and the drift velocity in simulation. The calculated drift velocity is taken from the correction map estimated in the laser simulation. The drift velocity in simulation is the drift velocity taken from the relation shown in Figure 26, corresponding to the E-field of the space charge simulation.

A set of representative resulting drift velocities and uncertainties measured with laser data is listed in Table 3.

Position (X, Y, Z) [cm]	$v_X \pm \text{stat.} \pm \text{syst.}$ ($\text{mm } \mu\text{s}^{-1}$)	$v_Y \pm \text{stat.} \pm \text{syst.}$ ($\text{mm } \mu\text{s}^{-1}$)	$v_Z \pm \text{stat.} \pm \text{syst.}$ ($\text{mm } \mu\text{s}^{-1}$)
(30.58, -4.65, 518.40)	$1.060 \pm 0.001 \pm 0.0002$	$0.001 \pm 0.015 \pm 0.0000$	$0.001 \pm 0.001 \pm 0.0000$
(224.22, -4.65, 518.40)	$1.171 \pm 0.011 \pm 0.0002$	$-0.021 \pm 0.022 \pm 0.0000$	$-0.001 \pm 0.015 \pm 0.0000$
(122.30, -79.05, 518.40)	$1.086 \pm 0.012 \pm 0.0003$	$-0.046 \pm 0.003 \pm 0.0003$	$0.001 \pm 0.006 \pm 0.0000$
(122.30, 79.05, 518.40)	$1.101 \pm 0.002 \pm 0.0000$	$0.123 \pm 0.008 \pm 0.0000$	$0.002 \pm 0.011 \pm 0.0001$

Table 3. Representative local drift velocities measured using MicroBooNE laser data.

7.3 E-field Map measured from Laser Data

We calculate the absolute local E-field from the correction map derived from laser data as described in section 6.3.

Figure 34 presents the E-field map in components relative to the nominal E-field at central Z . They are $(E_X - E_0)/E_0[\%]$, $E_Y/E_0[\%]$ and $E_Z/E_0[\%]$. The nominal E-field in MicroBooNE is $E_0 = 273.9 \text{ V cm}^{-1}$ along the drift direction X . The value is derived from the high voltage applied between the cathode and the anode and the estimated drift length in liquid argon.

At central Z , the E-field component along the drift direction X is about 10% stronger than E_0 near the cathode and E_X is about 6% weaker than E_0 near the anode. The area with weaker E_X is slightly larger than the area with stronger E_X . In the upper region, E_Y is about 30 V cm^{-1} pointing upwards. In the lower region, E_Y is about 15 V cm^{-1} pointing downwards. E_Z is relatively small and flat at central Z , mostly within -2 V cm^{-1} to 2 V cm^{-1} . The lower most row in Y is empty due to lack of laser coverage.

The dominant contribution to the E-field distortion in MicroBooNE is space charge arising from cosmic rays. Muons from cosmic rays enter the TPC at a rate of $\sim 10 \text{ kHz}$. Positive charge builds up in the form of an ion cloud near the cathode. Ionizing electrons travelling from inside the ion cloud to the anode will be boosted in the E-field by the attraction of the ion clouds, so the E-field is stronger there. When ionizing electrons travel through the ion clouds, they are attracted from the ion clouds from both the $+X$ and $-X$ directions. When these reach equilibrium, E_X is close to E_0 . When the ionizing electrons travel further towards the anode, the attraction from the ion clouds pulls the electrons backwards. With the static E-field from the ion clouds in the opposite direction of E_0 , the total E_X is weaker due to distance. Similarly, ionizing electrons are attracted to the ion cloud in all directions, and indeed we observe E_Y pointing outwards in the upper and lower regions of the TPC. The asymmetry of E_Y in the upper and lower regions may be due to the cosmic ray muons entering the TPC at the top, with less ions created at the bottom. Additionally the poor laser coverage near the bottom may contribute to this. Furthermore, convection of the liquid argon inside the TPC can move ion charges. The E-field along the beam direction E_Z is very small and uniform, because the space charge distribution is almost symmetric with respect to the central Z .

The statistical uncertainty of the measured E-field obtained using laser data is achieved by propagating the statistical uncertainty from the correction map in the same way as is done for the velocity map. An example of the distribution of E-field component in a bin can be seen in Figure 35. We take the standard deviation from a fit to the distributions in every bin as the statistical uncertainty of the E-field measurement. In Figure 26, around the nominal E-field in MicroBooNE E_0 , and with E-field distortion up to 50 V cm^{-1} , the drift speed varies close to linearly with respect

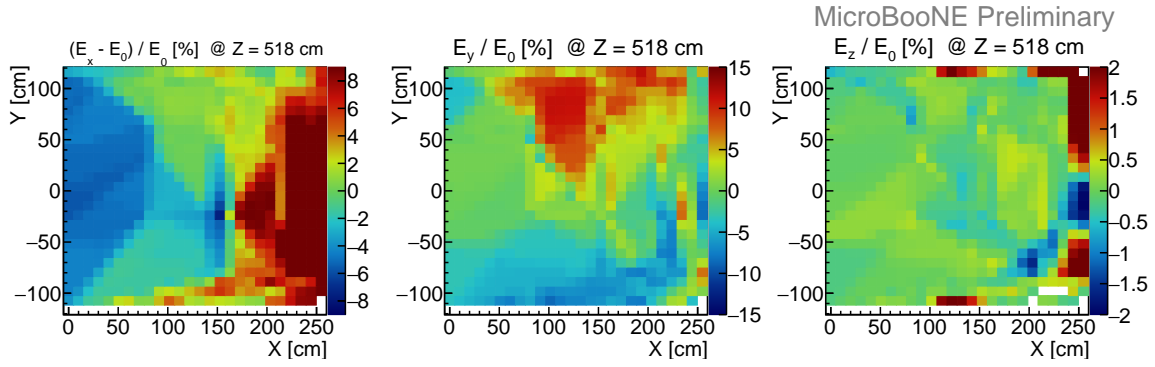


Figure 34. Relative E-field components (in percent) for the three coordinates $(E_X - E_0)/E_0[\%]$ (left), $E_Y/E_0[\%]$ (middle) and $E_Z/E_0[\%]$ (right) at a central slice in Z . The maximal relative E-field distortion is about 10%.

to the magnitude of the E-field. As the error propagation to the E-field shows Gaussian distributions in Figure 35 we use the values from the fit.

The statistical uncertainty in percentage of E_0 at central Z is shown in Figure 36. Typical statistical uncertainties of the E-field component in a bin are below 2% of E_0 .

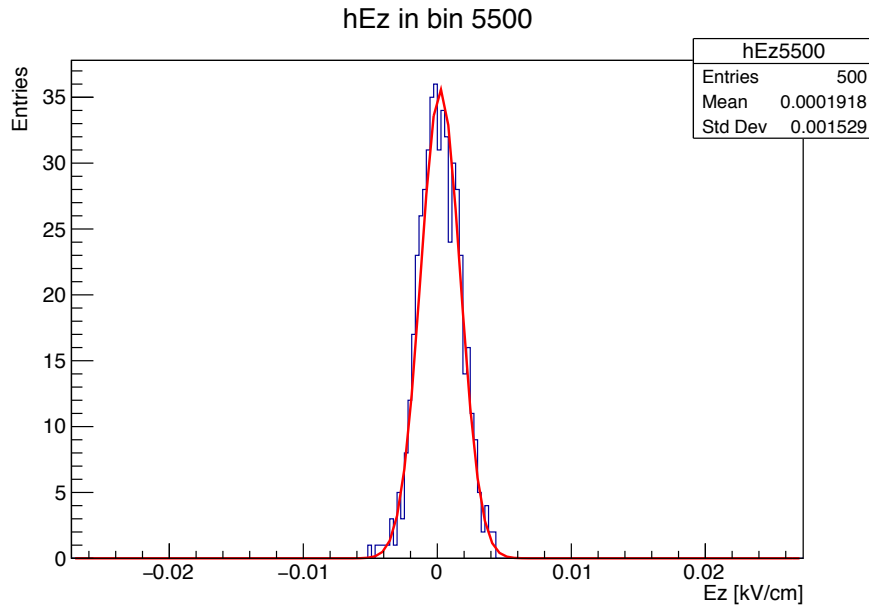


Figure 35. Distribution of the vertical E-field components E_Z for 500 initial correction maps used in the error propagation. The red line shows the Gauss function fitted to it.

The systematic uncertainty of the E-field measurement performed with laser data is also determined by the bias study using the laser simulation. The bias is defined as the difference of the simulated E-field (space charge simulation Section 6.4) and the calculated E-field using the laser simulation described in Section 5.5.2. The E-field in simulation is derived from the correction

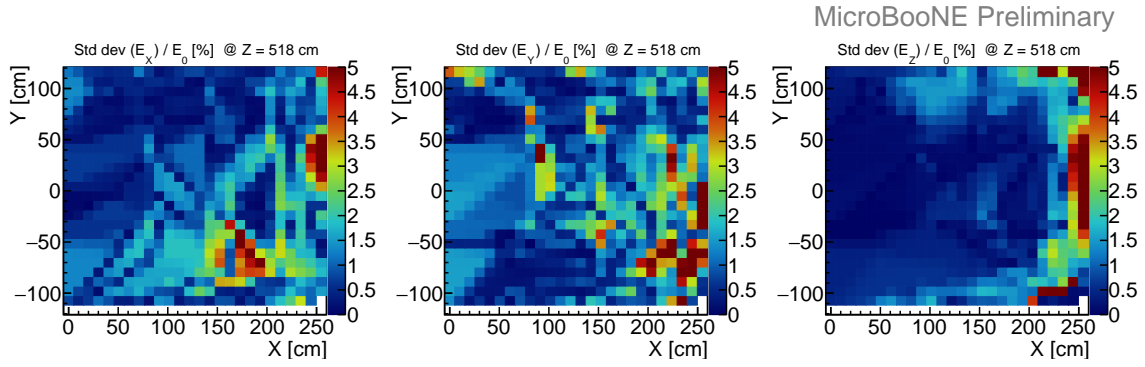


Figure 36. Standard deviation of the E-field components in each bin with respect to the nominal E-field in a central slice in Z . From left to right the three components are shown: $Std\ dev(E_X)/E_0[\%]$, $Std\ dev(E_Y)/E_0[\%]$ and $Std\ dev(E_Z)/E_0[\%]$. The deviations are mostly within 2% of the nominal E-field E_0 , with the exception of some bins. Here the standard deviation of the E-field in each bin is the statistical uncertainty of the E-field measurement by laser data.

map, based on the space charge simulation and is binned in (21, 21, 81) bins in (X, Y, Z) . We interpolate the simulated E-field map in the same binning as the calculated one. The deviations that we observe at the edge of the map are due to the tri-linear interpolation lacking surrounding cubes. This systematic uncertainty in percentage of the nominal E-field E_0 at central Z is shown in Figure 37. Typical systematic uncertainties in a bin are within -2% to 2% of E_0 .

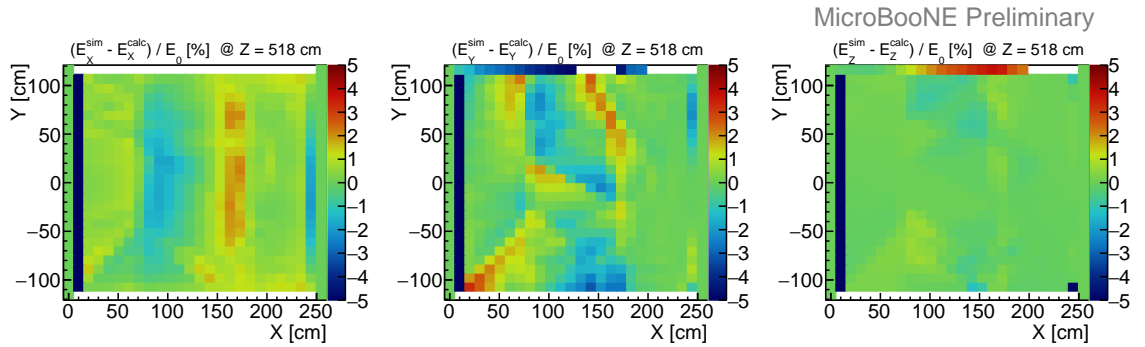


Figure 37. Bias of E-field components as determined from the laser simulation in percent of the nominal E-field at a central slice in Z . From left to right the three coordinates are shown: $(E_X^{sim} - E_X^{calculation})/E_0[\%]$, $(E_Y^{sim} - E_Y^{calculation})/E_0[\%]$ and $(E_Z^{sim} - E_Z^{calculation})/E_0[\%]$. The bias is mostly within 2% of E_0 . The bias of the E-field determined by the laser simulation in each bin is used as systematic uncertainty for the E-field measurement with laser data.

A set of representative E-field vectors measured by laser data is listed in Table 4. The values are presented as relative E-field distortions in components of $\Delta E_X = E_X - E_0$, $\Delta E_Y = E_Y$, $\Delta E_Z = E_Z$. The E-field distortion reaches $\sim 30\text{ V cm}^{-1}$, and the uncertainties are usually a few V cm^{-1} .

Position (X, Y, Z) [cm]	$\Delta E_X \pm \text{stat.} \pm \text{syst.} (\text{V cm}^{-1})$	$\Delta E_Y \pm \text{stat.} \pm \text{syst.} (\text{V cm}^{-1})$	$\Delta E_Z \pm \text{stat.} \pm \text{syst.} (\text{V cm}^{-1})$
(30.58, -4.65, 518.40)	$-14.76 \pm 0.30 \pm 1.06$	$0.13 \pm 3.75 \pm 0.06$	$0.13 \pm 0.35 \pm 0.01$
(224.22, -4.65, 518.40)	$30.70 \pm 4.90 \pm 1.09$	$-5.51 \pm 5.69 \pm 0.31$	$-0.20 \pm 3.81 \pm 0.01$
(122.30, -79.05, 518.40)	$-4.51 \pm 4.92 \pm 1.29$	$-11.45 \pm 0.84 \pm 1.33$	$0.19 \pm 1.53 \pm 0.03$
(122.30, 79.05, 518.40)	$2.23 \pm 0.71 \pm 0.29$	$30.85 \pm 1.95 \pm 0.17$	$0.55 \pm 2.85 \pm 0.72$

Table 4. Representative E-field distortions measured by laser data.

8 Time Dependency Studies

Time stability of the E-field in the TPC is a vital factor for deciding the frequency of the E-field measurements. It also provides an assessment of additional uncertainties of the E-field measurement for a single measurement which are not included in Section 6.3.

A time dependency study of the E-field for longer time scales of months or years will be part of an upcoming publication. The major source of the variation here would be the flux of cosmic rays.

In this section, we report the results of a time dependency study performed over a few-hours time scale. Over such times, contribution to the fluctuations in the E-field may come from the flux of cosmic rays and convection of LAr in the TPC. The LAr is constantly circulated through filters to keep the concentration of electronegative impurities low and additionally, there is convection through heat input through the cryostat.

To investigate the time dependency, we pulse the laser with the mirror set to point at a constant direction across the TPC in Z over a few hours. The frequency of the laser beam pulse is kept low at \sim mHz, so multi-photon ionization from the laser would not contribute to space charge. To avoid the possible uncertainties from laser track reconstruction, which is explained in Section 3.1, we conduct the time dependency study by looking at the raw waveform signals from the wire readout. If the E-field varies over time, the position (time in the waveform) of the charge deposition of the laser in the TPC also changes due to varied drift velocity and path. Thus, the position of the laser in each wire waveforms over time is a good representation of the time stability.

We observe the amplitude and the sampling time of the laser signals (peak) in the waveform, where the amplitude is measured in ADC counts and the time in sample ticks. From each raw waveform an ADC baseline, calculated for that waveform, is subtracted. The ADC unit is then converted to mV by a known calibration factor. The sample ticks are transformed to μ s by using the fact that every ADC sampling time takes 500 ns. The sampling time of the laser signals is taken with respect to the laser-trigger time, given by a diode in the laser boxes and recording the laser pulse emission. For this time dependency study only waveform signal from the collection plane are used.

First we show the variation of the peak sampling time from three typical wires. The middle plot in Figure 38 shows the overlap of 1500 laser pulses from downstream to upstream. The three wires correspond to different regions in the TPC. The top plot of Figure 38 shows one representative waveform for these three wires out of the 1500 laser events. The baselines of these three waveforms have already been corrected. As can be seen in the figure, the peak amplitudes of the laser signal in these three wires do not vary significantly. The slightly smaller peak amplitude of the first wire is

due to the fact that it represents a signal from the laser beam after it travelled in LAr for more than 10 m, (3.75 m more than than the next selected wire. The waveforms are fitted by Gaussian functions and the mean of the Gaussian is defined as peak sampling time. The bottom plot of Figure 38 shows the histograms of peak sampling times in each of the selected wires. Each histogram only contains peak sampling times of the waveforms from a single wire. The peak sampling time in the top plot contributes to one entry in the corresponding histogram. We then perform a further Gaussian fit to each histogram and obtain $\mu_1 = 943.63 \mu\text{s}$, $\sigma_1 = 1.52 \mu\text{s}$, $\mu_2 = 974.92 \mu\text{s}$, $\sigma_2 = 1.83 \mu\text{s}$, $\mu_3 = 993.95 \mu\text{s}$, $\sigma_3 = 1.70 \mu\text{s}$ for the three wires, respectively. The width σ of the Gaussian distribution indicates the spread in laser position in the TPC, which reflects the stability of the E-field. In these studies the stability of the laser track itself can be neglected due to mechanical constraints and considerations.

Among all the wires of the collection plane, the largest variation from the Gaussian fit of the waveforms is found to be $\sigma_{\text{max}} = 1.93 \mu\text{s}$. On that wire, the best fit gives $\mu = 956.23 \mu\text{s}$, corresponding to a spread of the laser position on a single wire of $\sigma_{\text{max}}^{\hat{}} = 2.2 \text{ mm}$. This also implies a 0.2% change in drift velocity along the X direction (v_X) and in turn a time related variation of the E-field is less than 0.3%.

Figure 39 shows the peak sampling time of the laser signal for more wires over time. The horizontal axis is the laser triggering time with respect to the first laser pulse. The vertical axis shows the relative peak sampling time for the different wires. For simplicity of display, we skip 100 wires ($\sim 30 \text{ cm}$) in between every wire that is shown. The baseline of the peak sampling time is incremented by $10 \mu\text{s}$ from wire to wire that is shown. The pattern of the peak sampling time over the presented 2 hour range shows correlations with respect to the neighbouring wires in time. This implies that the time related variations are position dependent. Thus, the variations in peak sampling time are likely to be indeed related to the E-field.

In the area with the largest distortion we find variations along the X of about 2 mm, $0.004 \text{ mm } \mu\text{s}^{-1}$ and 1.8 V cm^{-1} in spatial displacement, drift velocity and E-field. This is not considered as significant and thus the E-field in the TPC is found to be stable over a few-hours timescale.

9 Possible Future Improvements

To further improve calibration measurements using UV laser-based systems in LArTPCs, we describe potential improvements to both hardware and analysis techniques, to be applied in future experiments. The most impactful consideration for future detectors is maximizing laser coverage. The calculated E-field map covers about 75% of MicroBooNE's active volume with the dominant restriction resulting from the hardware set-up. The limited availability of feedthroughs in the cryostat leads to the current mechanical placement of the laser heads and the mirrors.

9.1 Hardware Improvements: Future Design of Laser Systems

SBND [3], the near detector in Short-Baseline Neutrino (SBN) program, will also employ a LAr TPC and make use of a UV-laser system. In this case, the laser system contains two laser sub-systems in each TPC module. They penetrate the TPC field-cage rings and thus the steerable cold mirrors are inside the TPC active volume. The cold mirrors are located in the top corners, and therefore the E-field distortions due to the mirrors are expected to be small. In SBND the light

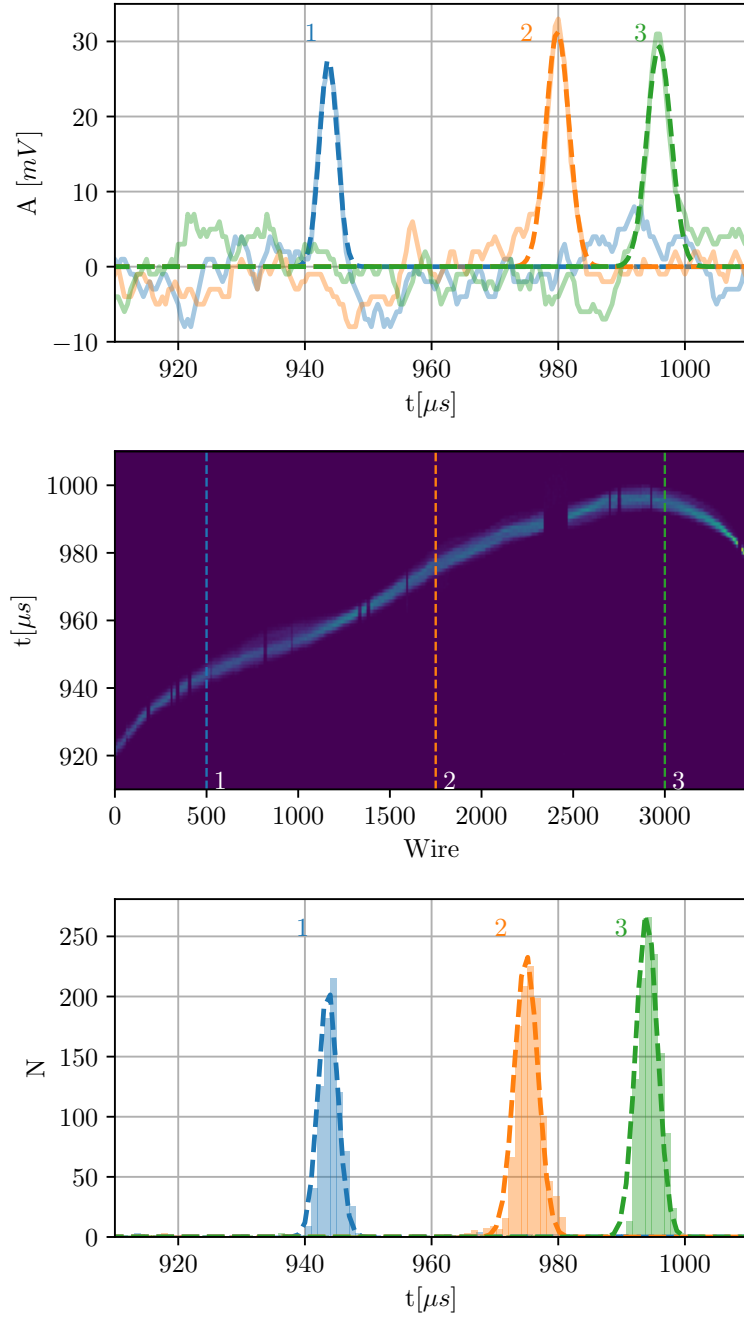


Figure 38. Top: Example of raw waveforms of selected wires in an event: wire 500 (blue, labelled as case **1**), wire 1750 (orange, labelled as case **2**) and wire 3000 (green, labelled as case **3**). Each waveform is fitted by a Gaussian and the central value of the Gaussian defines the peak sampling time. **Middle:** Overlap of 1500 laser pulses. The tracks are nearly straight with a vertical displacement of about 6.6 cm over a track lengths of 10.4 m. The horizontal axis in the figure is the wire number and the vertical axis is the drift time. The color illustrated is the sum of amplitude of the 1500 waveform. Gaps in the color stream (laser beam) correspond to unresponsive wires in the MicroBooNE read out. The positions of the three wires **1**, **2** and **3** are indicated in the plot. **Bottom:** Histogram of peak sampling time on wire **1**, **2** and **3**. Each histogram has 1500 entries and each entry is the peak sampling time of a waveform on that wire from a laser pulse. Gaussian fits to each histogram result in means and standard deviations of $\mu_1 = 943.63 \mu\text{s}$, $\sigma_1 = 1.52 \mu\text{s}$, $\mu_2 = 974.92 \mu\text{s}$, $\sigma_2 = 1.83 \mu\text{s}$ and $\mu_3 = 993.95 \mu\text{s}$, $\sigma_3 = 1.70 \mu\text{s}$.

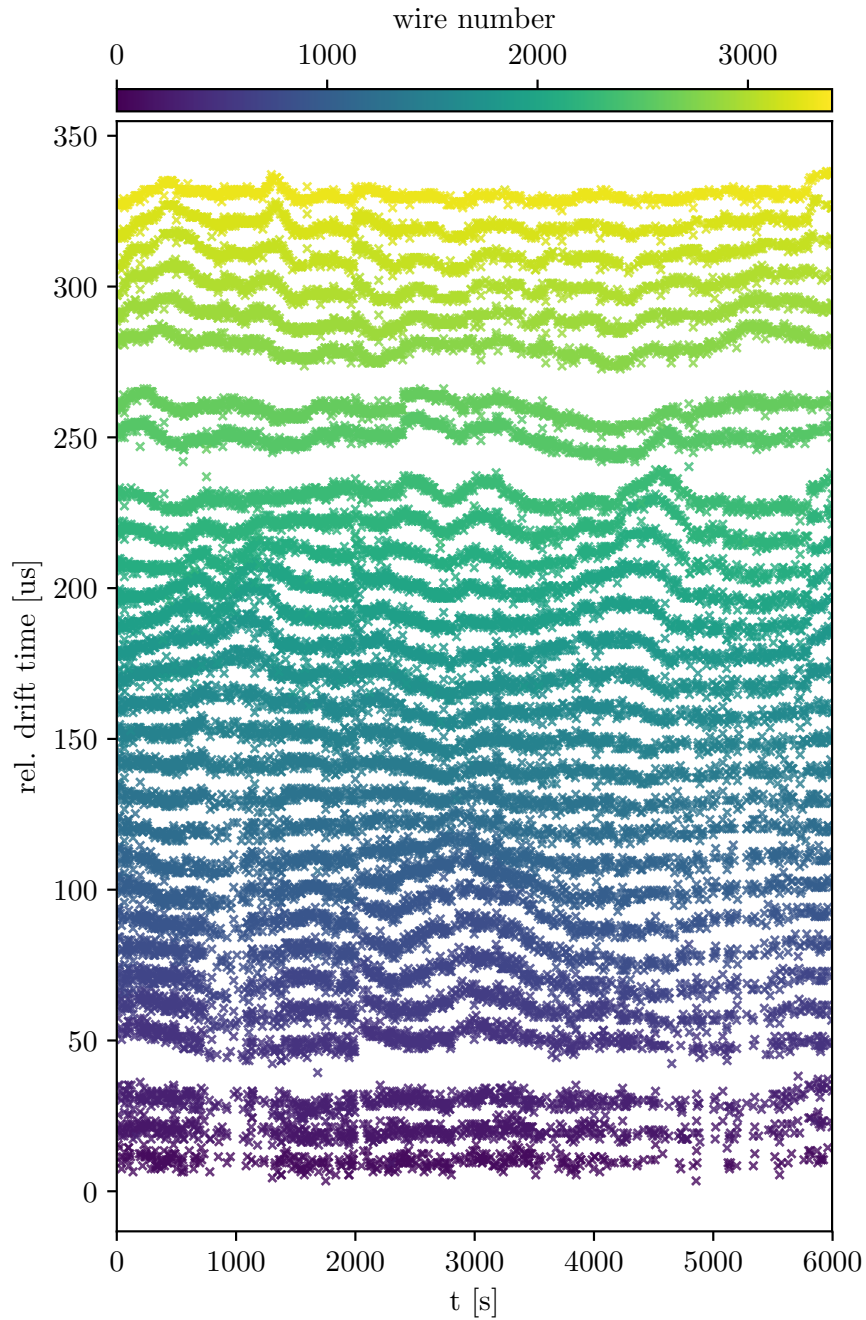


Figure 39. Time evolution of the peak sampling time on different wires. The horizontal axis is the time with respect to the first laser pulse. The vertical axis shows the relative peak sampling time of different wires. The same color indicates that peak sampling time is from the same wire. We skip 100 wires in between every 2 wires that are shown. For display reasons, the baseline of the peak sampling time on each displayed wire are increased by $10\ \mu\text{s}$ recursively.

detection system is placed behind the anode planes, and the cold laser mirrors are close to the anode planes. Therefore, the area near the cathode can be scanned by the laser without risk of pulsing the laser into the wavelength shifting plates directly. Instead of placing the cold mirrors vertically at half height like in MicroBooNE, SBND plans to place them in the top corners to shorten the length of laser path in LAr. Thus, the laser pulse energy would not decrease much before reaching the TPC. In MicroBooNE, laser beams pointing downwards tend to be reconstructed as laser tracks with degraded quality. This is due to the large incident angle of laser beams on the dichroic mirrors, which are optimized for 45° incidence angle. The laser incident angle is zero when the cold mirrors are facing vertically upwards in MicroBooNE. The reflectance of the dichroic mirror is relatively low when the incident angle is significantly above 45°. In SBND, the laser incident angle is zero when the steerable mirror is facing vertically downwards. To scan the whole TPC module, the steerable cold mirror turns horizontally and vertically and the laser incident angle is always within 0° to 45°. Since the range of scanning angle is smaller, it would take less time to conduct a full TPC laser scan. Moreover, SBND plans to use dichroic mirrors with coatings which are adjusted for the refractive index of LAr.

Similar improvements are also planned for the UV-laser systems that is foreseen to be installed in the DUNE far detector.

With even more complete and efficient laser scans, the spatial displacement calculation would have higher accuracy. This will lead to a larger region of validity and a more accurate measurement of the local drift velocity and the local E-field.

9.2 Analysis Improvements: Maxwell-Faraday constraints

The integral form of the Maxwell-Faraday equation is $\oint_{\partial\Sigma} \mathbf{E} \cdot d\mathbf{l} = \int_{\Sigma} \frac{\partial \mathbf{B}}{\partial t} \cdot d\mathbf{A}$. In MicroBooNE, there is no magnetic field varying over time in the entire TPC active volume, so the integral of the E-field along an arbitrary chosen contour $\partial\Sigma$ should result in $\oint_{\partial\Sigma} \mathbf{E} \cdot d\mathbf{l} = 0$.

This constraint can be used to extend the range of the E-field measurement. The E-field map is voxelized over the TPC active volume. Simplifying the following calculation by only selecting paths $\partial\Sigma$ of integral along X, Y, Z , one also simplifies the E-field in a bin by taking E_X, E_Y and E_Z to be the same as the E-field in the bin centre over the whole bin. If there is only one unknown E-field component along $\partial\Sigma$, then this unknown component can be determined by $\oint_{\partial\Sigma} \mathbf{E} \cdot d\mathbf{l} = 0$. The calculated value can further be fed into the calculation iteratively. However, a few difficulties need to be solved before this constraint becomes a practical addition to the determination of the E-field map. It is not trivial to choose a $\partial\Sigma$ with only one unknown E-field component in a bin, because the target bins are unlikely to be surrounded by other bins with known E-field. All three components of the E-field E_X, E_Y and E_Z have to be known at a bin centre to claim knowledge of the local E-field. If there are more than two unknown local E-field components, one needs the same amount of path integrals to reveal the unknown local E-field components. Depending on the geometry of the available local E-field, some E-field components may be impossible to fill with Maxwell-Faraday constraints. This introduces additional difficulties for choosing the paths of $\oint_{\partial\Sigma} \mathbf{E} \cdot d\mathbf{l}$. Furthermore, the uncertainties on the local E-field component determined by a Maxwell-Faraday constraint is cumulative along the path. It may also be necessary not to take the local E-field as constant in a 10 cm \times 10 cm \times 10 cm bin.

The Maxwell-Faraday constraint could also be considered as a smoothness tool for the E-field map, if most of the bins are filled with the calculated E-field. Similarly, the local E-field is simplified to be constant in a bin and $\partial\Sigma$ to be along X, Y, Z . From every bin, a close path integral of the E-field is initiated. The E-field components in that bin can be derived by requesting that $\oint_{\partial\Sigma} \mathbf{E} \cdot d\mathbf{l} = 0$, without using the originally calculated E-field in that bin. By repeating this calculation with different paths one can form a distribution of E-field components in that bin. In the region of the E-field where there already is appreciable bias, the bias could be further increased by the Maxwell-Faraday constraint and possibly propagate to the whole E-field. If the initial E-field calculation, however, is close to the constrained value, this method can provide a preferred value with a more accurate local E-field component in that bin.

9.3 Alternate displacement map determinations

Alternate calculations of the displacement vectors have been investigated in order to improve the coverage and continuity of the E-field map in MicroBooNE.

As a first option, instead of using track sets from two laser sub-systems in the track iteration, we used an evenly mixed track set. Any available tracks from the scan have neighbouring tracks in the other track set. With this configuration, the shared coverage of two track sets is recovered. At the same time, the problem falls back to the track angle dependence. In the track iteration step, the displacement vector of a track point is interpolated from the displacement vectors of four surrounding track points. The surrounding track points are likely from the neighbouring tracks, which have similar track angles as the track point is from. We found the calculated displacement maps to be similar to the ones calculated without track iteration. However, the bias in the central region, which is covered by lasers from both sub-systems, was larger compared to the bias of the default displacement maps. The use of mixed track sets did not show improvements in coverage here and was not adopted.

Figure 5 shows how the true laser track-ends and the reconstructed laser track-ends are not necessarily associated by the displacement vectors. Based on this we attempted to use a linear-stretch projection instead of the closest-point projection to calculate the initial displacement vectors. It can be observed in the figure that the true laser track-ends and the reconstructed laser track-ends are not necessarily connected by the displacement vectors. The linear stretch projection associates the first reconstructed point to the closest end of the truth track, and the last reconstructed point to the other end of the truth track. The rest of the reconstructed track points are then projected to the truth track by length proportion. Assuming N as the number of track points in a reconstructed track, the length of track fragment in between the first and the second reconstructed point can be estimated by the distance in between them, and it is noted as L_1^R . Similarly, the fragment length in between the n -th and the $(n + 1)$ -th point can also be estimated by the distance in between them L_n^R . The reconstructed track length is estimated by the sum of all the fragments lengths, i.e. $L_{\text{track}}^R = \sum_{i=1}^{N-1} L_i^R$. We take this estimation for the track length to avoid normalization bias. The true laser track length L_{track}^T is the length of a straight line from the laser entry to the laser exit points. From Equation 9.1 we know the distance L_n^T , which is the length in between the n th true point and the $(n + 1)$ -th true point. With the n th true point in Section 5.5.3 meaning the point on the true track which is associated to the n -th reconstructed point. Knowing the first true point is the

laser entry point, all the other true points on the same track can be deduced recursively.

$$\frac{L_n^R}{L_{\text{track}}^R} = \frac{L_n^T}{L_{\text{track}}^T} \quad (9.1)$$

Again, the correction vectors are determined from the reconstructed track points and the corresponding true track points, and the distortion vectors go from the true track points to the corresponding reconstructed track points. The calculation of displacement vectors then follows by iterating over tracks. The linear-stretch projection performs relatively well in the toy simulation. The bias at edge Z reduces to less than a centimetre. However, the bias increases significantly when it is applied to the laser simulation. The foundation of the linear-stretch projection is the assumption that reconstructed tracks are complete. Otherwise, the linear proportion would be incorrect to represent the projection from reconstructed points to true points. A few broken tracks can therefore significantly degrade the displacement map by track iteration and interpolation.

To solve this issue, we tried combining the linear-stretch and the closest-point projections. The track selection guarantees that the selected tracks start from a position close to the true track entries, while there is no strict restriction on the track ends. Based on this selection, we use the linear-stretch projection for the start of the tracks and closest-point projection for the rest part of the tracks. The distance from the track starts to the transit points of the two projection methods is tested to be 40 cm and 100 cm. Two different transit distances are chosen based on the appearance of the triangle-like region. The resulting bias, however, was larger compared to the map which only uses closest-point projection, especially when the transit distance is 100 cm. This could be due to the fact that the number of points in a track after subset division is not sufficient to provide a good estimation of track length. Thus, the displacement vectors calculated by linear proportion projection did not agree well with the displacement vectors calculated by closest point projection in the transit region with respect to the positions of track points. And therefore also this combination failed to recover the use of the UV-laser in the TPC regions which are difficult to cover in the UV-laser implementation in MicroBooNE. Furthermore, the linear-stretch projection amplifies any misalignment cumulatively. Laser beams have uncertainties of a few mm and the laser entry or exit could thus not be reconstructable, depending on E-field distortion. For example, the ionizing electrons at the laser entry or exit points may drift away from the TPC active volume. The association of the first and the last reconstructed point to the laser entry and exit would then be lost. Thus, linear-stretch projection was not employed in this analysis. However, it might be beneficial to other setups, for example, if the entry and exit points can be determined more precisely.

10 Conclusion

It is vital for large LAr TPCs, such as MicroBooNE and the future experiments SBND and DUNE, to have precise E-field maps in order to minimize the uncertainty in neutrino event reconstruction, since the E-field of the TPC directly impacts both particle tracking and calorimetry.

A fully steerable laser system which allows remote control has been successfully operated for the first time in MicroBooNE. We have observed over 10 m long laser tracks across the TPC in the Z direction. The design can be used as a reference for future experiments, such as SBND and

DUNE, which plan similar systems. We have also developed a general methodology to determine the E-field, drift velocity and spatial displacement in TPCs, using the laser system.

By introducing laser beams along known paths, the spatial displacement of tracks introduced by E-field distortions can be measured. We determined the E-field map of the MicroBooNE TPC by backtracking the ionizing electron drifts in the TPC E-field and comparing to derived space points to those reconstructed using a nominal E-field. The measured E-field distortion reaches $\sim 30 \text{ V cm}^{-1}$ for a nominal field of 274 V cm^{-1} , and the uncertainties from this method are within a few V cm^{-1} . The largest contribution to the distortions are consistent with the expectation from space charge induced by cosmic ray muons. Simulations have been used to validate different parts of the methodology. In addition, we used simulations to extract systematic uncertainties on the E-field where detector data is not available. A time dependency study showed that the E-field distortion is stable over a time scale of a few hours.

The extent of the E-field map that can be measured with the MicroBooNE setup is limited by the coverage of the laser system. This can be improved in future experiments, with better integration of the laser system with initial TPC design. An independent method was developed based on cosmic ray muons, which is part of a separate publication. This latter method covers portions of the TPC where the laser lacks coverage and thus the two methods are complementary. MicroBooNE plans to use the information obtained by both methods to obtain a merged data-driven E-field map.

Another limiting factor is found to be the track reconstruction algorithms, which have not been optimized for laser tracks which are broader and yield larger energy depositions than a MIP deposition. Improvements here will lead to a reduced systematic uncertainty of the spatial displacement map, to which the E-field measurement is sensitive.

Acknowledgments

This document was prepared by the MicroBooNE collaboration using the resources of the Fermi National Accelerator Laboratory (Fermilab), a U.S. Department of Energy, Office of Science, HEP User Facility. Fermilab is managed by Fermi Research Alliance, LLC (FRA), acting under Contract No. DE-AC02-07CH11359. MicroBooNE is supported by the following: the U.S. Department of Energy, Office of Science, Offices of High Energy Physics and Nuclear Physics; the U.S. National Science Foundation; the Swiss National Science Foundation; the Science and Technology Facilities Council of the United Kingdom; and The Royal Society (United Kingdom). Additional support for the laser calibration system and cosmic ray tagger was provided by the Albert Einstein Center for Fundamental Physics (Bern, Switzerland).

References

- [1] DUNE collaboration, B. Abi et al., *The DUNE Far Detector Interim Design Report Volume 1: Physics, Technology and Strategies*, [1807.10334](#).
- [2] MicroBooNE collaboration, R. Acciarri et al., *Design and Construction of the MicroBooNE Detector*, *JINST* **12** (2017) P02017, [[1612.05824](#)].
- [3] MicroBooNE, LAR1-ND, ICARUS-WA104 collaboration, M. Antonello et al., *A Proposal for a Three Detector Short-Baseline Neutrino Oscillation Program in the Fermilab Booster Neutrino Beam*, [1503.01520](#).

- [4] A. Ereditato, I. Kreslo, M. L'Åijthi, C. Rudolf von Rohr, M. Schenk, T. Strauss et al., *A Steerable UV Laser System for the Calibration of Liquid Argon Time Projection Chambers*, *JINST* **9** (2014) T11007, [[1406.6400](#)].
- [5] J. Sun, D. Cao and J. Dimmock, *Investigating Laser-Induced Ionization of Purified Liquid Argon in a Time Projection Chamber*, *Nucl. Instrum. Meth.* **A370** (1996) 372–376.
- [6] B. Rossi et al., *A Prototype Liquid Argon Time Projection Chamber for the Study of UV Laser Multi-Photonic Ionization*, *JINST* **4** (2009) P07011, [[0906.3437](#)].
- [7] I. Badhrees et al., *Measurement of the Two-Photon Absorption Cross-Section of Liquid Argon with a Time Projection Chamber*, *New J. Phys.* **12** (2010) 113024, [[1011.6001](#)].
- [8] A. Ereditato, C. C. Hsu, S. Janos, I. Kreslo, M. Messina, C. Rudolf von Rohr et al., *Design and Operation of ARGONTUBE: a 5 m Long Drift Liquid Argon TPC*, *JINST* **8** (2013) P07002, [[1304.6961](#)].
- [9] MICROBooNE collaboration, C. Adams et al., *Ionization Electron Signal Processing in Single Phase LArTPCs. Part I. Algorithm Description and Quantitative Evaluation with MicroBooNE Simulation*, *JINST* **13** (2018) P07006, [[1802.08709](#)].
- [10] MICROBooNE collaboration, C. Adams et al., *Ionization Electron Signal Processing in Single Phase LArTPCs. Part II. Data/Simulation Comparison and Performance in MicroBooNE*, *JINST* **13** (2018) P07007, [[1804.02583](#)].
- [11] E. L. Snider and G. Petrillo, *LArSoft: Toolkit for Simulation, Reconstruction and Analysis of Liquid Argon TPC Neutrino Detectors*, *J. Phys. Conf. Ser.* **898** (2017) 042057.
- [12] MICROBooNE collaboration, R. Acciarri et al., *The Pandora Multi-Algorithm Approach to Automated Pattern Recognition of Cosmic-Ray Muon and Neutrino Events in the MicroBooNE Detector*, *Eur. Phys. J.* **C78** (2018) 82, [[1708.03135](#)].
- [13] GEANT4 collaboration, S. Agostinelli et al., *GEANT4: A Simulation Toolkit*, *Nucl. Instrum. Meth.* **A506** (2003) 250–303.
- [14] C. Jamin, S. Pion and M. Teillaud, *3D Triangulation Data Structure*, in *CGAL User and Reference Manual*. CGAL Editorial Board, 4.13 ed., 2018.
- [15] C. Jamin, S. Pion and M. Teillaud, *3D Triangulations*, in *CGAL User and Reference Manual*. CGAL Editorial Board, 4.13 ed., 2018.
- [16] S. Amoruso et al., *Analysis of the Liquid Argon Purity in the ICARUS T600 TPC*, *Nucl. Instrum. Meth.* **A516** (2004) 68–79.
- [17] W. Walkowiak, *Drift Velocity of Free Electrons in Liquid Argon*, *Nucl. Instrum. Meth.* **A449** (2000) 288–294.
- [18] THE MICROBooNE COLLABORATION collaboration, *Study of Space Charge Effects in MicroBooNE*, MICROBooNE-NOTE-1018-PUB ed., 2016.